

A physical model for the [C II]–FIR deficit in luminous galaxies

Desika Narayanan^{1,2★} and Mark R. Krumholz^{3,4,†}

¹*Department of Physics and Astronomy, Haverford College, 370 Lancaster Ave, Haverford, PA 19041, USA*

²*Department of Astronomy, University of Florida, 211 Bryant Space Sciences Center, Gainesville, 32611 FL, USA*

³*Research School of Astronomy and Astrophysics, Australian National University, Canberra, ACT 2611, Australia*

⁴*Kapteyn Astronomical Institute, University of Groningen, the Netherlands*

Accepted 2016 December 8. Received 2016 December 6; in original form 2016 January 21

ABSTRACT

Observations of ionized carbon at 158 μm ([C II]) from luminous star-forming galaxies at $z \sim 0$ show that their ratios of [C II] to far-infrared (FIR) luminosity are systematically lower than those of more modestly star-forming galaxies. In this paper, we provide a theory for the origin of this so-called [C II] deficit in galaxies. Our model treats the interstellar medium as a collection of clouds with radially stratified chemical and thermal properties, which are dictated by the clouds' volume and surface densities, as well as the interstellar radiation and cosmic ray fields to which they are exposed. [C II] emission arises from the outer, H I-dominated layers of clouds, and from regions where the hydrogen is H_2 but the carbon is predominantly C^+ . In contrast, the most shielded regions of clouds are dominated by CO, and produce little [C II] emission. This provides a natural mechanism to explain the observed [C II]–star formation relation: galaxies' star formation rates are largely driven by the surface densities of their clouds. As this rises, so does the fraction of gas in the CO-dominated phase that produces little [C II] emission. Our model further suggests that the apparent offset in the [C II]–FIR relation for high- z sources compared to those at present epoch may arise from systematically larger gas masses at early times: a galaxy with a large gas mass can sustain a high star formation rate even with a relatively modest surface density, allowing copious [C II] emission to coexist with rapid star formation.

Key words: astrochemistry – ISM: molecules – ISM: structure – galaxies: ISM.

1 INTRODUCTION

The $^2P_{3/2} - ^2P_{1/2}$ fine structure transition of singly ionized carbon¹ (hereafter [C II]) at $\lambda = 158 \mu\text{m}$ is one of the most luminous emission lines in star-forming galaxies, and a principal coolant of the neutral interstellar medium (ISM; Malhotra et al. 1997; Luhman et al. 1998; Nikola et al. 1998). Indeed, [C II] can account for ~ 0.1 –1 per cent of the far-infrared (FIR) luminosity in galaxies (Stacey et al. 1991). The line is excited mainly via collisions with electrons, neutral hydrogen (H I) and molecular hydrogen (H_2), with the relatively low critical densities of ~ 44 , $\sim 3 \times 10^3$ and $\sim 6 \times 10^3 \text{ cm}^{-3}$, respectively (Goldsmith et al. 2012).² This, combined with the relatively low ionization potential of 11.3 eV, means that [C II] emission can arise from nearly every phase in the ISM.

For present-epoch galaxies, ground-based observations of [C II] are challenging owing to telluric water vapour absorption in the Earth's atmosphere. Early work with the Kuiper Airborne Observatory (KAO) and *Infrared Space Observatory* (ISO) presented evidence of a relationship between galaxies' [C II] luminosities and their global star formation rates (SFRs). For example, KAO observations of 14 nearby galaxies by Stacey et al. (1991) revealed ratios of $[\text{C II}]/^{12}\text{CO}$ ($J=1-0$) emission similar to those found for Galactic star-forming regions, providing an indirect link between the [C II] line luminosity and SFR (via the $\Sigma_{\text{SFR}} - \Sigma_{\text{CO}}$ relation in galaxies). Later observations utilizing ISO by Leech et al. (1999) and Boselli, Lequeux & Gavazzi (2002) established bona fide relations between [C II] and the SFR in $z \sim 0$ systems. More recently, the launch of the *Herschel Space Observatory*, combined with other high-resolution ultraviolet and infrared observations, has established a firm [C II]–SFR relation in nearby galaxies (de Looze et al. 2011; Sargssyan et al. 2012; Pineda, Langer & Goldsmith 2014; Herrera-Camus et al. 2015). Cosmological zoom simulations of galaxy formation by Olsen et al. (2015) have suggested that the majority of the [C II] emission that drives this relationship originates in molecular gas or photodissociation regions (PDRs) in giant clouds, providing a natural explanation for why [C II] should be correlated with star formation.

* E-mail: desika.narayanan@gmail.com

† Blaauw Visiting Professor.

¹ Throughout this paper, we will use [C II] when referring to the observable emission line, and C^+ when discussing ionized carbon within the context of chemical networks.

² At kinetic temperatures of 8000, 100 and 100 K, respectively.

This said, even since the early days of *ISO* observations of galaxies, it has been clear that the SFR–[C II] relationship breaks down in the $z \sim 0$ galaxies with the highest infrared luminosities. Put quantitatively, the [C II]/FIR luminosity ratio decreases with increasing infrared luminosity, such that ultraluminous infrared galaxies (ULIRGs; galaxies with $L_{\text{IR}} \geq 10^{12} L_{\odot}$) emit roughly ~ 10 per cent of the [C II] luminosity that would be expected if they had the same [C II]/FIR ratios as galaxies of lower FIR luminosity (Malhotra et al. 1997, 2001; Luhman et al. 1998, 2003). The evidence for the so-called [C II]–FIR deficit has grown stronger in the *Herschel* era. Graciá-Carpio et al. (2011) showed that the [C II]–FIR deficit is uncorrelated with galaxies’ nuclear activity level, and that similar deficits with respect to FIR luminosity may exist in other nebular lines as well. Díaz-Santos et al. (2013) added significantly to existing samples via a survey of [C II] emission from ~ 250 $z \sim 0$ luminous infrared galaxies (LIRGs; $L_{\text{IR}} \geq 10^{11} L_{\odot}$), and confirmed these conclusions. Other evidence for this deficit in local systems has come from Beirão et al. (2010), Croxall et al. (2012) and Farrah et al. (2013).

At high redshift, the evidence for a [C II]–FIR deficit in galaxies is more mixed. While there have been a number of [C II] detections in $L_{\text{IR}} \geq 10^{12} L_{\odot}$ galaxies at $z \sim 2$ –6 (see Casey, Narayanan & Cooray 2014 for a recent compendium of these data and review of high- z detections), and certainly many exhibit depressed [C II]/FIR luminosity ratios, many additionally show elevated [C II]/FIR luminosity ratios compared to local galaxies with a similar infrared luminosity (e.g. Iono et al. 2006; Stacey et al. 2010; Swinbank et al. 2012; Wagg et al. 2012; Rawle et al. 2013; Riechers et al. 2013; Wang et al. 2013; Rigopoulou et al. 2014; Brisbin et al. 2015).

In this paper, we aim to provide a physical explanation for the origin of the [C II]–FIR deficit in heavily star-forming galaxies in the local Universe, and the more complex pattern found at high redshift. We do this by developing analytic models for the structure of giant clouds in galaxies. We combine chemical equilibrium networks and numerical radiative transfer models with these cloud models to develop a picture for how [C II] emission varies both as a function of cloud radius, as well as with galactic environment.

Our central argument is relatively straightforward. Consider a galaxy with a two-phase neutral ISM comprised of H_2 and H I . As the surface density of the gas in the galaxy grows, its SFR rises. However, the increased surface density also increases the ability of the hydrogen to shield itself from dissociating Lyman–Werner band photons (Krumholz, McKee & Tumlinson 2008, 2009a; McKee & Krumholz 2010), causing the $\text{H}_2/\text{H I}$ ratio to rise. Within clouds, owing to cosmic ray and ultraviolet radiation-driven chemistry effects, C^+ is prevalent in the PDR but is significantly depleted in the H_2 core. As a result, the typical decreasing sizes of PDRs in galaxies of increasing SFR result in proportionally lower [C II] luminosities.

In what follows, we present a numerical model that shows these physical and chemical trends explicitly. In Section 2, we describe the model, while in Section 3 we outline the main results, including the luminosities of [C II] in molecular and atomic gas. In Section 4, we discuss some applications of this model, including its utility for high-redshift galaxies and ISM calorimetry. We additionally discuss the relationship of our model to other theoretical models in this area, as well as uncertainties in our model. Finally, we summarize in Section 5.

2 MODEL DESCRIPTION

Our goal is to explain the observed relationship between [C II] 158 μm emission and SFR, for which FIR emission is a proxy. However, the physical state of a galaxy’s ISM obviously depends

on more than its SFR. Quantities such as the volume density, chemical state and temperature play a role as well. We therefore develop a minimal model for a galactic ISM as a whole, and then use that model to compute both SFR and [C II] emission.

We idealize a galaxy as a collection of spherical, virialized star-forming clouds. (Since we are mainly concerned with luminous galaxies whose ISM are dominated by molecular gas, we do not include a non-star-forming diffuse atomic component in our models, but we consider the possible impact of such a component on our results in Section 4.5.1.) Because, in our minimalist model, the galaxy is made up of a collection of spherical clouds, it does not itself have a specific or derived size. Instead, it is agnostic to the physical mechanism that generates the cloud surface densities.

Each cloud consists of several radial zones that each have distinct column densities, and that are chemically and thermally independent from one another. To calculate the line emission from a galaxy, our first step is to compute the density, column density and velocity dispersion of each of these clouds. We do so following the procedure outlined in Section 2.1. We then use the code Derive the Energetics and Spectra of Optically Thick Interstellar Clouds (DESPOTIC; Krumholz 2013a,b) to compute the chemical state (Section 2.2), temperature (Section 2.3) and level populations (Section 2.4) in every layer of the cloud. The entire model is iterated to convergence as outlined in Section 2.5, and, once convergence is reached, we can compute the total [C II] 158 μm luminosity.

For convenience, we have collected various parameters that appear in our model in Table 1, and drawn a schematic of the processes to be described in Fig. 1.

2.1 Cloud physical structure

The chemical and thermal states of clouds, both in our model and in reality, will depend upon their volume and column densities, as well as their velocity dispersions. The first step in our calculation is therefore to model the relationship between these quantities and galaxies’ SFRs. To this end, let Σ_{g} be the surface density of an idealized spherical cloud. The inner part of this cloud will be H_2 dominated and the outer layers, which are exposed to the unattenuated interstellar radiation field (ISRF), will be dominated by H I ; the specified surface density Σ_{g} includes both of these zones. The H_2 -dominated region comprises a fraction f_{H_2} of the total cloud mass. Krumholz et al. (2008, 2009a), Krumholz, McKee & Tumlinson (2009b) and McKee & Krumholz (2010, hereafter collectively referred to as KMT) show that the molecular mass fraction for such a cloud obeys

$$f_{\text{H}_2} \approx 1 - \frac{3}{4} \frac{s}{1 + 0.25s} \quad (1)$$

for $s < 2$ and $f_{\text{H}_2} = 0$ for $s \geq 2$. Here $s = \ln(1 + 0.6\chi + 0.01\chi^2)/(0.6\tau_{\text{c}})$, where $\chi = 0.76(1 + 3.1Z^{0.365})$, the dust optical depth of the cloud at frequencies in the Lyman–Werner band is $\tau_{\text{c}} = 0.066\Sigma_{\text{g}}/(M_{\odot} \text{pc}^{-2}) \times Z'$ and Z' is the metallicity normalized to the solar metallicity. We assume $Z' = 1$ for all model clouds, and thus f_{H_2} is a function of Σ_{g} alone.

We relate the atomic and molecular regions via their density contrast. Specifically, following KMT, we define

$$\phi_{\text{mol}} = \frac{\rho_{\text{H}_2}}{\rho_{\text{H I}}}, \quad (2)$$

where ρ_{H_2} and $\rho_{\text{H I}}$ are the densities in the molecular atomic zones, respectively, and we adopt a fiducial value $\phi_{\text{mol}} = 10$. This is based on the typical molecular cloud densities of $n_{\text{mol}} \approx 100 \text{ cm}^{-3}$, and densities of giant H I clouds of $n_{\text{CNM}} \approx 10 \text{ cm}^{-3}$ (Elmegreen &

Table 1. Parameters used in cloud models.

Variable	Definition	Value
Parameters for cloud physical properties (Section 2.1)		
ϵ_{ff}	Dimensionless star formation efficiency	0.01
α_{vir}	Cloud virial ratio	1.0
ρ_{MW}	Molecular cloud density normalization	$2.34 \times 10^{-22} \text{ g cm}^{-3}$
N	Star formation law index	2
ϕ_{mol}	Ratio of molecular to atomic density	10
M_{gal}	Galaxy gas mass	$1 \times 10^9 - 2 \times 10^{11} M_{\odot}$
Σ_{g}	Cloud surface density	$\sim 50 - 5000 M_{\odot} \text{ pc}^{-2}$
Parameters for cloud thermal and chemical properties		
N_{zones}	Number of radial zones in model clouds	16
χ_{FUV}	FUV ISRF	$1.0 \times \text{SFR} / (M_{\odot} \text{ yr}^{-1})$
ξ_{-16}	Cosmic ray ionization rate	$0.1 \times \text{SFR} / (M_{\odot} \text{ yr}^{-1})$
α_{GD}	Gas–dust coupling coefficient	$3.2 \times 10^{-34} \text{ erg cm}^3 \text{ K}^{-3/2}$
$\sigma_{\text{d}, 10}$	Dust cross-section to 10 K thermal radiation	$2.0 \times 10^{-26} \text{ cm}^2 \text{ H}^{-1}$
T_{CMB}	Cosmic microwave background temperature	2.73 K
Z'_{d}	Dust abundance relative to solar	1
β_{d}	Dust opacity versus frequency index	2
$A_{\text{V}}/N_{\text{H}}$	Visual extinction per column	$4 \times 10^{-22} Z' \text{ mag cm}^2$
OPR	Ortho-to-para ratio in H_2 gas	0.25

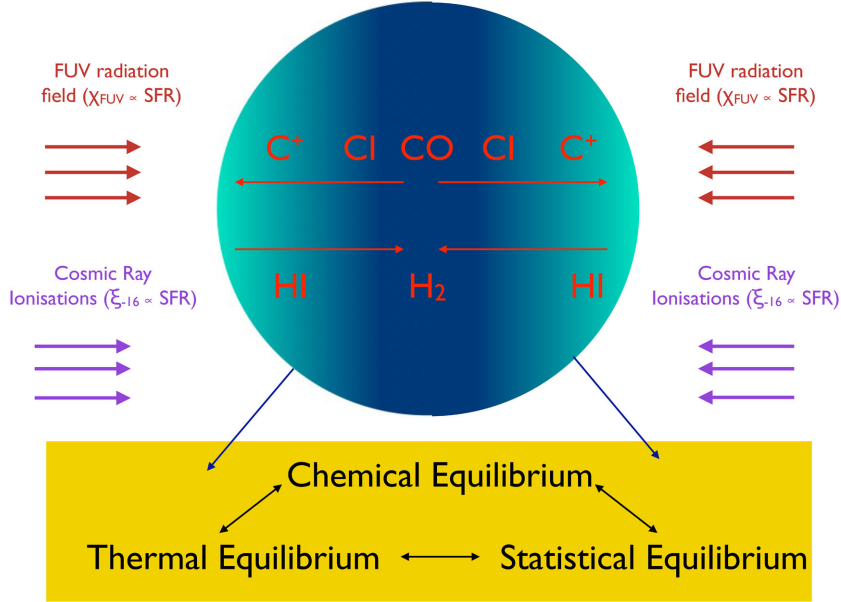


Figure 1. Schematic showing the basic model employed here. Clouds are assumed to be radially stratified spheres illuminated by both a far-UV (FUV) radiation field and cosmic rays. Both the FUV field and cosmic ray ionization rates scale with the galaxy SFR. The thermal, chemical and level population balances are calculated simultaneously as each depends on one another. Our galaxies are comprised of individual clouds such as these that make up the entirety of the neutral gas in our model.

Elmegreen 1987; McKee & Ostriker 2007). With this choice and a bit of algebra, one can show that the total cloud mass and radius can be expressed in terms of Σ_{g} and ρ_{H_2} as

$$M_{\text{c}} = \frac{9}{16} \pi [f_{\text{H}_2} + \phi_{\text{mol}}(1 - f_{\text{H}_2})]^2 \frac{\Sigma_{\text{g}}^3}{\rho_{\text{H}_2}^2} \quad (3)$$

$$R_{\text{c}} = \frac{3}{4} \left(1 + \phi_{\text{mol}} \frac{1 - f_{\text{H}_2}}{f_{\text{H}_2}} \right) \frac{\Sigma_{\text{g}}}{\rho_{\text{H}_2}}. \quad (4)$$

We can also express the velocity dispersion of the cloud in terms of these two variables via the virial theorem. Specifically, we have the

ratio of the kinetic to gravitational energy given by the dimensionless virial parameter:

$$\alpha_{\text{vir}} = \frac{5\sigma_{\text{c}}^2 R_{\text{c}}}{GM_{\text{c}}}, \quad (5)$$

where σ_{c} is the velocity dispersion and α_{vir} is the virial ratio (Bertoldi & McKee 1992). Thus

$$\sigma_{\text{c}} = \sqrt{\frac{3\pi}{20} \alpha_{\text{vir}} f_{\text{H}_2}^2 \left(1 + \phi_{\text{mol}} \frac{1 - f_{\text{H}_2}}{f_{\text{H}_2}} \right) \frac{G \Sigma_{\text{g}}^2}{\rho_{\text{H}_2}}}. \quad (6)$$

We adopt a fiducial value for the virial ratio $\alpha_{\text{vir}} = 1$, typical of observed molecular clouds (e.g. Dobbs, Burkert & Pringle 2011; Dobbs et al. 2013; Heyer & Dame 2015). Recalling that f_{H_2} is a function of Σ_{g} alone, we have now succeeded in writing the cloud mass, radius and velocity dispersion in terms of Σ_{g} and ρ_{H_2} alone, and we have therefore reduced our model to a two-parameter family.

To proceed further, we now bring star formation into the picture. Consider a galaxy with a total ISM mass $M_{\text{gal}} = N_{\text{c}}M_{\text{c}}$, where N_{c} is the number of star-forming clouds in the galaxy. At all but the lowest metallicities, stars form only in the molecular region of the ISM (e.g. Glover & Mac Low 2011; Krumholz, Leroy & McKee 2011; Krumholz 2012). Thus, the total star formation rate of the galaxy is given by

$$\text{SFR} = \epsilon_{\text{ff}} \frac{f_{\text{H}_2} M_{\text{gal}}}{t_{\text{ff}}}, \quad (7)$$

where t_{ff} is the free-fall time, and given by

$$t_{\text{ff}} = \sqrt{\frac{3\pi}{32 G \rho_{\text{H}_2}}}, \quad (8)$$

and the quantity ϵ_{ff} is the fraction of the molecular mass converted to stars per free-fall time. Observations strongly constrain this to be within a factor of a few of 1 per cent (Krumholz & Tan 2007; Krumholz, Dekel & McKee 2012; Krumholz 2014), so we adopt $\epsilon_{\text{ff}} = 0.01$ as a fiducial value.³

Since f_{H_2} is a function of Σ_{g} alone in our model, we now have the total galaxy SFR in terms of three parameters: Σ_{g} , M_{gal} and ρ_{H_2} . We can eliminate the last of these on empirical grounds. Individual clouds in the Milky Way have $\Sigma_{\text{g}} \approx 100 \text{ M}_{\odot} \text{ pc}^{-2}$ and $\rho_{\text{H}_2} \approx 100 \mu_{\text{H}} \text{ cm}^{-3}$, where $\mu_{\text{H}} = 2.34 \times 10^{-24} \text{ g}$ is the mean mass per H nucleus for gas that is 90 per cent H and 10 per cent He by mass (Dobbs et al. 2013; Heyer & Dame 2015). The remaining question is how ρ_{H_2} scales as we vary Σ_{g} ; we assume that it does not vary with M_{gal} at fixed Σ_{g} , since variations of this form correspond simply to a galaxy having a smaller or larger star-forming disc. To derive this relationship, we note that observations of galaxies over a large range in surface densities show that the SFR surface density is well correlated with the gas surface density (Kennicutt & Evans 2012), $\Sigma_{\text{SFR}} \propto \Sigma_{\text{g}}^N$, when the SFR and gas surface densities measured over $\sim 1 \text{ kpc}$ scales. The exact value of the index N is debated in the literature, and is dependent on the exact sample, fitting method, and the value assumed to convert CO line luminosity (the most common method used to measure Σ_{g} in extragalactic observations) to H_2 gas mass (Bigiel et al. 2008; Blanc et al. 2009; Narayanan et al. 2011a,b, 2012a; Shetty et al. 2013a; Shetty, Kelly & Bigiel 2013b). We adopt a fiducial value $N = 2$, motivated by theoretical studies that suggest such a relation for LIRGs and ULIRGs when considering a CO– H_2 conversion factor that varies with ISM physical conditions (Narayanan et al. 2012a). Since we also have $\Sigma_{\text{SFR}} \propto \Sigma_{\text{g}}/t_{\text{ff}}$, we immediately have $t_{\text{ff}} \propto \Sigma_{\text{g}}^{1-N}$, and thus $\rho_{\text{H}_2} \propto \Sigma_{\text{g}}^{2(N-1)}$. Combining

³ We pause here to note an important subtlety, which is that ϵ_{ff} , while it can be referred to as a ‘star formation efficiency’, is not the same as the observational efficiency $L_{\text{IR}}/M_{\text{H}_2}$ (or its areal equivalent) sometimes used in the literature (e.g. Daddi et al. 2010; Graciá-Carpio et al. 2011; Genzel et al. 2012). The latter is a measure of the depletion time (the time required to convert the gas to stars), which is not constant, and which some authors have argued is bimodal, though Narayanan et al. (2012a) argue that this conclusion is an artefact of adopting a bimodal CO– H_2 conversion factor. However, while the depletion time is non-constant, Krumholz et al. (2012) show that the data are fully consistent with the dimensionless SFR per free-fall time ϵ_{ff} being constant.

this scaling with the Milky Way normalization described above, we arrive at our fiducial scaling between ρ_{H_2} and Σ_{g} :

$$\rho_{\text{H}_2} = \rho_{\text{MW}} \left(\frac{\Sigma_{\text{g}}}{100 \text{ M}_{\odot} \text{ pc}^{-2}} \right)^{2(N-1)} \quad (9)$$

with $\rho_{\text{MW}} = 100 \mu_{\text{H}}$ and $N = 2$. We discuss how changing either of the coefficient or index of this relation would affect our results in Section 4.5. However, we note that this scaling produces reasonable values for the Milky Way: the ISM mass inside the Solar Circle is $M_{\text{gal}} \approx 2 \times 10^9 \text{ M}_{\odot}$ considering both H I (Wolfire et al. 2003) and H_2 (Heyer & Dame 2015), and using $\Sigma_{\text{g}} = 100 \text{ M}_{\odot} \text{ pc}^{-2}$ in equations (1), (7) and (8) gives a total SFR of $3.7 \text{ M}_{\odot} \text{ yr}^{-1}$, within a factor of a few of the consensus range of $1\text{--}2 \text{ M}_{\odot} \text{ yr}^{-1}$ derived by Robitaille & Whitney (2010) and Chomiuk & Povich (2011).

We have therefore succeeded in completely specifying our model for the physical structure of star-forming galaxies and the clouds within them in terms of two free parameters, Σ_{g} and M_{gal} . We take the former to be in the range $1.75 \leq \log \Sigma_{\text{g}} \leq 3.75 \text{ M}_{\odot} \text{ pc}^{-2}$, and the latter to be in the range $10^9 \leq M_{\text{gal}} \leq 10^{10} \text{ M}_{\odot}$ for local galaxies, and $\sim 10^{10}\text{--}10^{11} \text{ M}_{\odot}$ for high-redshift ones. The minimum in the surface densities is motivated by observations of nearby galaxies (e.g. Bolatto et al. 2008; Leroy et al. 2013), while the range in galaxy gas masses is constrained by surveys of galaxies near and far (Saintonge et al. 2011; Bothwell et al. 2013).

We convert between SFR and observed infrared luminosity employing the Murphy et al. (2011) conversion as summarized by Kennicutt & Evans (2012),

$$\log_{10}(L_{\text{IR}}(3\text{--}1100 \mu\text{m})) = \log_{10}(\text{SFR}) + 43.41. \quad (10)$$

This of course assumes that the contribution of AGN in observed galaxies to the infrared luminosity is negligible, which is not yet a settled question (e.g. Lutz 2014).

Finally, we report the typical range of derived properties of our model clouds. The densities range from $1.15 \leq \log_{10}(n_{\text{H}}) \leq 6.25$, cloud radii from $0.4 \leq R_{\text{c}} \leq 225 \text{ pc}$ and cloud masses from $3.4 \leq \log_{10}(M_{\text{c}}) \leq 6.6$. We note that these idealized spherical clouds are not intended to represent the true physical structure of real filamentary clouds (that obviously have a range of physical conditions); rather, they are meant to represent the mean physical state of emitting neutral gas in a given galaxy.

2.2 Chemical structure

As mentioned above, our clouds consist of radial layers, each chemically independent from one another. Each cloud contains N_{zone} zones, with a default $N_{\text{zone}} = 16$. We show in Appendix A that this is sufficient to produce a converged result. We assign each cloud a centre-to-edge column density of H nuclei $N_{\text{H}} = (3/4)\Sigma_{\text{g}}/\mu_{\text{H}}$; the factor of (3/4) is simply the difference between the mean column density and the centre-to-edge column density. In this model, we assign the i th zone (starting with $i = 0$) to cover the range of column densities from $[i/N_{\text{zone}}]N_{\text{H}}$ to $[(i+1)/N_{\text{zone}}]N_{\text{H}}$, with a mean column density $N_{\text{H},i} = [(i+1/2)/N_{\text{zone}}]N_{\text{H}}$. We calculate the mass in each zone from the column density range and the volume density, assuming spherical geometry.

In each zone, we must determine the chemical state of the carbon and oxygen atoms. These two species, either separately in atomic form or combined into CO, are the dominant coolants and line emitters. We adopt total abundances of $[\text{C}/\text{H}] = 2 \times 10^{-4}$ and $[\text{O}/\text{H}] = 4 \times 10^{-4}$ for C and O, respectively, consistent with their abundances in the Milky Way (Draine 2011). In principle, depending on the physical properties of the gas in each layer, the carbon

can be stored predominantly as C^+ , C or CO . Similarly, the hydrogen can be in atomic or molecular form in any given layer, and this chemical state of the H in turn affects that of the C and O . To model these effects, we compute the chemical state of each zone using the reduced carbon–oxygen chemical network developed by Nelson & Langer (1999) combined with the Glover & Mac Low (2007) non-equilibrium hydrogen chemical network,⁴ combined following the procedure described in Glover & Clark (2012). We summarize the reactions included in our network, and the rate coefficients we use for them, in Table 2. We refer readers to Glover & Clark (2012) for full details on the network and its implementation, but we mention here three choices that are specific to the model we use in this paper.

First, the network requires that we specify the strength of the unshielded ISRF. We characterize this in terms of the far-ultraviolet (FUV) radiation intensity normalized to the solar neighbourhood value, χ_{FUV} . We assume that χ_{FUV} is proportional to a galaxy’s SFR normalized to the $1 M_{\odot} \text{ yr}^{-1}$ SFR of the Milky Way (Robitaille & Whitney 2010; Chomiuk & Povich 2011): $\chi_{FUV} = \text{SFR}/(M_{\odot} \text{ yr}^{-1})$. Thus, more rapidly star-forming galaxies have more intense radiation fields, which in turn drive corresponding changes in the chemistry and thermodynamics.

Secondly, we must compute the amount by which all photochemical reaction rates are reduced in the interiors of clouds by shielding of the ISRF. The `DESPOTIC` implementation of the Glover & Clark (2012) network that we use includes reductions in the rates of all photochemical reactions by dust shielding, and reductions in the rates of H_2 and CO dissociation by self-shielding and (for CO) H_2 cross-shielding. We characterize dust shielding in terms of the visual extinction $A_V = (1/2)(A_V/N_H)N_H$, where the ratio (A_V/N_H) is the dust extinction per H nucleus at V band (Table 1). The factor of $(1/2)$ gives a rough average column density over the volume of the cloud. We evaluate the reduction in the H_2 dissociation rate using the shielding function of Draine & Bertoldi (1996), which is a function of the H_2 column density and velocity dispersion; for the latter, we use the value given by equation (6), while for the former we use $N_{H_2} = x_{H_2} N_H$, where x_{H_2} is the abundance of H_2 molecules per H nucleus in the zone in question; note that each zone is independent, so we do not use information on the chemical composition of outer zones to evaluate x_{H_2} , a minor inconsistency in our model. Similarly, we compute the reduction in the CO photodissociation rate using an interpolated version of the shielding function tabulated by van Dishoeck & Black (1988), which depends on the CO and H_2 column densities. We evaluate the CO column density as $N_{CO} = x_{CO} N_H$, in analogy with our treatment of the H_2 column. We determine both abundances x_{H_2} and x_{CO} by iterating the network to convergence – see Section 2.5.

⁴ By using the Glover & Mac Low (2007) model for hydrogen chemistry, we are folding an inconsistency into our model. Specifically, to determine the bulk physical properties of our model clouds, including the SFRs, we utilize the KMT model to decompose the ISM phases into neutral hydrogen and molecular. This is unavoidable as the networks require knowledge of the background radiation field and cosmic ray ionization rate, both of which likely depend on the SFR and thus the H_2 fraction. To be fully consistent, we would be required to iterate between chemistry and star formation, which would be quite computationally expensive. Hereafter in the paper, all hydrogen phase abundances that we quote derive from what is explicitly calculated in the chemical equilibrium network. However, the level of inconsistency is generally small, in that the H_2 fraction that results from the explicit chemical modelling never deviates that strongly from the KMT prediction, varying by a maximum of a factor of ~ 2 within the surface density range of interest.

Thirdly, we must also specify the cosmic ray primary ionization rate ζ . The value of this parameter even in the Milky Way is significantly uncertain. Recent observations suggest a value $\zeta \sim 10^{-16} \text{ s}^{-1}$ in the diffuse ISM (Neufeld et al. 2010; Indriolo et al. 2012), but if a significant amount of the cosmic ray flux is at low energies, the ionization rate in the interiors of molecular clouds will be lower due to shielding; indeed, a rate as high as 10^{-16} s^{-1} appears difficult to reconcile with the observed low temperatures of ~ 10 K typically found in molecular gas (Narayanan & Davé 2012; Narayanan et al. 2012a). For this reason, we adopt a more conservative value of $\zeta = 10^{-17} \text{ s}^{-1}$ as our fiducial choice for the Milky Way. We discuss how this choice influences our results in Section 4.3. We further assume that the cosmic ray ionization rate scales linearly with the total SFR of a galaxy, so our final scaling is $\zeta_{-16} = 0.1 \times \text{SFR}/(M_{\odot} \text{ yr}^{-1})$, where $\zeta_{-16} \equiv \zeta/10^{-16} \text{ s}^{-1}$. Note that this choice of scaling too is significantly uncertain, and others are plausible.⁵

2.3 Thermal state of clouds

The third component of our model is a calculation of the gas temperature, which we compute independently for each zone of our model clouds. We find the temperature by balancing the relevant heating and cooling processes, as well as energy exchange with dust. Following Goldsmith (2001), the processes we consider are photoelectric and cosmic ray heating of the gas, line cooling of the gas by C^+ , C , O and CO , heating of the dust by the ISRF and by a thermal infrared field, cooling of the dust by thermal emission, and collisional exchange between the dust and gas. We also include cooling by atomic hydrogen excited by electrons via the Lyman α and Lyman β lines and the two-photon continuum, using interpolated collisional excitation rate coefficients (Osterbrock & Ferland 2006, table 3.16); these processes become important at temperatures above ~ 5000 K, which are sometimes reached in the outer zones of our clouds. Formally,

$$\Gamma_{pe} + \Gamma_{CR} - \Lambda_{\text{line}} - \Lambda_H + \Psi_{gd} = 0 \quad (11)$$

$$\Gamma_{\text{ISRF}} + \Gamma_{\text{thermal}} - \Lambda_{\text{thermal}} - \Psi_{gd} = 0. \quad (12)$$

Terms denoted by Γ are heating terms, those denoted by Λ are cooling terms, while the gas–dust energy exchange term Ψ_{gd} can have either sign depending on the gas–dust temperature difference; our convention is that a positive sign corresponds to dust being hotter than the gas, leading to a transfer from dust to gas.

As with the chemical calculation, we solve these equations using the `DESPOTIC` code, and we refer readers to Krumholz (2013a) for a full description of how the rates for each of these processes are computed. The parameters we adopt are as shown in Table 1. Note that the line cooling rate depends on the statistical equilibrium calculated as described in Section 2.4.

2.4 Statistical equilibrium

The final part of our model is statistical equilibrium within the level populations of each species. The `DESPOTIC` code computes these using the escape probability approximation for the radiative transfer

⁵ For example, Papadopoulos (2010) and Bisbas, Papadopoulos & Viti (2015) assume that cosmic ray intensity scales as the volume density of star formation rather than the total rate of star formation; which assumption is closer to reality depends on the extent to which cosmic rays are confined by magnetic fields and subject to losses as they propagate through a galaxy.

problem. Formally, we determine the fraction f_i of each species in quantum state i by solving the linear system

$$\sum_j f_j \left[q_{ji} + \beta_{ji}(1 + n_{\gamma,ji})A_{ji} + \beta_{ij} \frac{g_i}{g_j} n_{\gamma,ij} A_{ij} \right] = f_i \sum_k \left[q_{ik} + \beta_{ik}(1 + n_{\gamma,ik})A_{ik} + \beta_{ki} \frac{g_k}{g_i} n_{\gamma,ki} A_{ki} \right] \quad (13)$$

subject to the constraint $\sum f_i = 1$. Here A_{ij} is the Einstein coefficient for spontaneous transitions from state i to state j , g_i and g_j are the degeneracies of the states,

$$n_{\gamma,ij} = \frac{1}{\exp(\Delta E_{ij}/k_B T_{\text{CMB}}) - 1} \quad (14)$$

is the photon occupation number of the cosmic microwave background at the frequency corresponding to the transition between the states, E_{ij} is the energy difference between the states and β_{ij} is the escape probability for photons of this energy. We compute the escape probability for each shell independently, assuming a spherical geometry.

The escape probabilities computed include the effects of both resonant and dust absorption – see Krumholz (2013a) for details. Finally, q_{ij} is the collisional transition rate between the states, which is given by $q_{ij} = f_{\text{cl}} n_{\text{H}} k_{\text{H},ij}$ or $q_{ij} = f_{\text{cl}} n_{\text{H}_2} k_{\text{H}_2,ij}$ in the H I and H₂ regions, respectively; the quantities $k_{\text{H},ij}$ and $k_{\text{H}_2,ij}$ are the collision rate coefficients, n_{H} and n_{H_2} are the number densities of H atoms or H₂ molecules, and f_{cl} is a factor that accounts for the enhancement in collision rates induced by turbulent clumping.

All the Einstein collisional rate coefficients required for our calculation come from the Leiden Atomic and Molecular Database (Schöier et al. 2005). In particular, we make use of the following collision rate coefficients: C⁺ with H (Launay & Roueff 1977; Barinova et al. 2005), C⁺ with H₂ (Wiesenfeld & Goldsmith 2014), C with H (Launay & Roueff 1977), C with He (Staemmler & Flower 1991), C with H₂ (Schroder et al. 1991), O with H (Abrahamsson, Krems & Dalgarno 2007), O with H₂ (Jaquet et al. 1992) and CO with H₂ (Yang et al. 2010).

2.5 Convergence and computation of the emergent luminosity

Calculation of the full model proceeds via the following steps. First, we compute the physical properties of each cloud following the method given in Section 2.1. Armed with these, we guess an initial temperature, chemical state and set of level populations for each layer in the cloud. We then perform a triple-iteration procedure, independently for each zone. The outermost loop is to run the chemical network (Section 2.2) to convergence while holding the temperature fixed. The middle loop is to compute the temperature holding the level populations fixed (Section 2.3). The innermost loop is to iterate the level populations of each species to convergence (Section 2.4). We iterate in this manner until all three quantities – chemical abundances, temperature and level populations – remain fixed to within a certain tolerance, at which point we have found a consistent chemical, thermal and statistical state for each zone.

Once the level populations are in hand, it is straightforward to compute the observable luminosity in the [C II] 158 μm line, or in any other transition. The total luminosity per unit mass produced in a line produced by molecules or atoms of species S transitioning between states i and j , summed over each zone, is

$$L_{ij}/M = \mu_{\text{H}}^{-1} x_S \beta_{ij} \left[(1 + n_{\gamma,ij}) f_i - \frac{g_i}{g_j} n_{\gamma,ij} f_j \right] A_{ij} E_{ij}, \quad (15)$$

where x_S is the abundance of the species and f_i and β_{ij} are the level populations and escape probabilities in each layer. Each zone n has a mass M_n , computed from its range of column densities, and the total luminosity of the N_c clouds in the entire galaxy is simply

$$L_{ij} = N_c \mu_{\text{H}}^{-1} A_{ij} E_{ij} \sum_n M_n x_{S,n} \beta_{ij,n} \cdot \left[(1 + n_{\gamma,ij}) f_{i,n} - \frac{g_i}{g_j} n_{\gamma,ij} f_{j,n} \right], \quad (16)$$

where $x_{S,n}$, $f_{i,n}$ and $\beta_{ij,n}$ are the abundance, level population fraction and escape probability in the n th zone of our model clouds.

2.6 Sample results

Before moving on to our results for [C II] emission, in this section we provide a brief example of the thermal and chemical properties that our models produce. These will provide the reader with some intuition for how the physical, thermal and chemical properties of our model clouds vary with galaxy infrared luminosity, or mean cloud surface density. For this example, we consider a galaxy with a gas mass of $M_{\text{gal}} = 10^9 M_{\odot}$ (i.e. similar to the Milky Way), and we vary the surface density Σ_g within the range specified in Table 1. For each value of Σ_g , we derive an SFR (equation 7) and thus an FIR luminosity, and we run the chemical–thermal–statistical network to equilibrium following the procedure described in Section 2.5. We summarize the resulting cloud properties as a function of FIR luminosity and Σ_g in Fig. 2, where we show the cloud mean densities, fractional chemical abundances for a few species, gas kinetic temperatures and ISM heating/cooling rates as a function of cloud surface density (and galaxy infrared luminosity).

The fractional abundance subpanels of Fig. 2 summarize the central arguments laid out in this paper. As the total cloud surface densities rise, so does the typical mass fraction of gas in the H₂ phase (Krumholz et al. 2008), owing to the increased ability of hydrogen to self-shield against dissociating Lyman–Werner band photons. This point is especially pertinent to our central argument. At a fixed galaxy mass, increased gas surface densities lead to increased SFRs. In these conditions, the molecular-to-atomic ratio in giant clouds increases. At the same time, with increasing cloud surface density (or galaxy SFR), C⁺ abundances decline, and CO abundances increase. This owes principally to the role of dust column shielding CO from photodissociating radiation. The fraction of the cloud that is dominated by C⁺ hence decreases with increasing cloud surface density.

For the temperature, we discriminate between H₂ and H I gas in clouds, and plot the mass-weighted values for each phase. We additionally show the CO luminosity-weighted gas temperature with the dashed line, as this is the temperature that most closely corresponds to observations. At low cloud surface densities, the CO dominates the cool ($T \sim 15$ K) inner parts of clouds, though the warmer outer layers are dominated by C I and C⁺. The bulk of the mass is at these warmer temperatures, and the heating is dominated by the grain photoelectric effect. At higher cloud surface densities, the bulk of the cloud is dominated by CO. Here, the grain photoelectric effect is less effective owing to increased A_V , but the impact of cosmic ray ionisations and energy exchange with dust is increased.

3 RESULTS

In the model that we develop, the [C II]–FIR deficit in galaxies principally owes to a combination of atomic PDRs serving as the

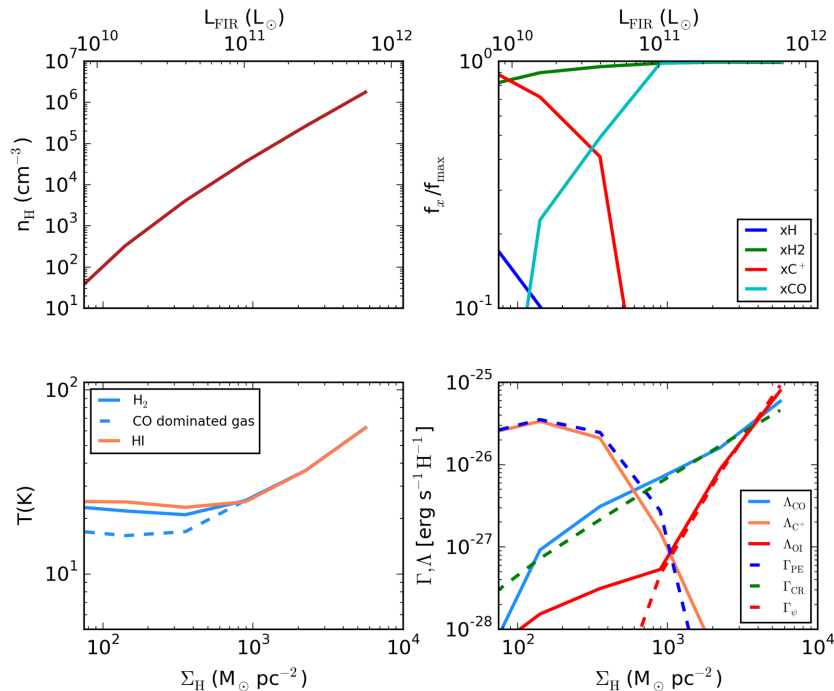


Figure 2. Physical properties of model clouds inside a galaxy of $M_{\text{gal}} = 10^9 M_{\odot}$ as a function of cloud surface density. These include volume density (top left), chemical abundances (top right), gas kinetic temperature (bottom left) and heating/cooling rates (bottom right). All quantities shown are mass-weighted averages, with the exception that in the gas kinetic temperature panel the different lines correspond to temperatures weighted by H I mass, H₂ mass and CO luminosity, respectively.

dominant site of C⁺ in galaxies and a decreasing atomic-to-molecular fraction in galaxies of increasing luminosity. In this section, we lay the case for this argument in detail.

3.1 Carbon-based chemistry

We begin with the instructive question: how is CO in clouds typically formed and destroyed? The principal formation channels for CO are via neutral–neutral reactions with CH_x and OH_x (CH_x and OH_x refer to variables that agglomerate molecules CH, CH₂, etc., and similarly for OH). CO is destroyed in the ISM via both cosmic rays and ultraviolet radiation. The molecule is directly destroyed most efficiently via interactions with ionized helium, He⁺, which is created via cosmic ray ionizations of neutral He. At the same time, FUV radiation can also reduce CO abundances via a variety of channels: it can directly destroy CO, as well as prevent its formation via the photodissociation of CO’s main formation reactants, C I, CH_x and OH_x. Once carbon is in neutral atomic form, UV radiation can ionize C I in order to form C⁺.

Opposing CO dissociation and ionization (and consequently the formation of C⁺) are the surface density and volumetric density of the cloud. To understand the role of the surface density, consider the photoreactions in Table 2. The dissociation rates are only linearly dependent on the ultraviolet radiation field strength, but exponentially decrease with increased A_V . In particular, increased surface densities prevent the dissociation and ionization of CH_x, OH_x and CO molecules, as well as C I.

Increased volumetric densities, n_{H} , also promote neutral atom and molecule formation, and prevent the formation of C⁺. Again, consider the photoionization of neutral carbon. The reaction rates for photodissociations and photoionizations are density independent. However, the recombination and molecular formation rates within

the ion–molecule, ion–atom and neutral–neutral reactions all scale linearly with density. Hence, given sufficient density, recombination and molecule formation outpace the ionization rates.

The carbon-based chemistry in clouds in galaxies is therefore set by a competition between the SFR of the galaxy, and the density and surface density of clouds. The SFR controls the cosmic ray ionization rate, as well as the ultraviolet flux. As a result, all else being equal, increased SFRs result in decreased molecular CO abundances, and increased C I and C⁺ abundances.

In order to provide the reader with some intuition as to how these effects drive carbon-based chemistry, in Figs 3 and 4, we show the CO and C⁺ abundances for a grid of model cloud densities and surface densities given a range of SFRs (and FUV fluxes and cosmic ray ionization rates that scale, accordingly). Note that these cloud models are principally for the purposes of the illustration of dominant physical effects, and therefore have not been constructed via the methods in Section 2 (meaning that the SFR, Σ_{SFR} , densities and surface densities are not all interconnected, nor is there a multiphase breakdown of these clouds; they are of a single ISM phase). The effects of increased cosmic ray fluxes and FUV radiation field strengths via increased SFR on the carbon-based chemistry are clear. At low SFRs, even relatively low n_{H} and Σ_{H} gas is sufficiently well shielded that the carbon can exist in molecular (CO) form. Consequently, C⁺ is confined to the most diffuse gas at low SFRs. At higher SFRs, the situation is reversed. Increased χ_{FUV} and cosmic ray ionization rates dissociate CO and ionize C, thereby increasing C⁺ abundances in clouds with a large range in physical conditions. C⁺ is destroyed, and C I and CO are most efficiently formed, when the volume density and surface density of the cloud simultaneously increase.

The numerical experiments represented in Figs 3 and 4 give some intuition as to how carbon will behave in different physical

Table 2. Coefficients adopted for our chemical network, following Glover & Clark (2012). In this table, ζ is the cosmic ray primary ionization rate, χ_{FUV} is the normalized FUV radiation field strength, A_V is the visual extinction, $x_{\text{H}} = n_{\text{H}}/n$ is the H abundance, $x_{\text{H}_2} = n_{\text{H}_2}/n$ is the H₂ abundance, $T_4 = T/(10^4 \text{ K})$, $\ln(T_e) = \ln(8.6173 \times 10^{-5} \times T/\text{K})$. Note that this network includes several super-species: CH_x agglomerates CH, CH₂, etc., and similarly for OH_x, and M and M⁺ agglomerate a number of metallic species with low ionization potentials (e.g. Fe, Si).

Reaction	Rate coefficient
Cosmic ray reactions [$\text{s}^{-1} \text{ molecule}^{-1}$]:	
$\text{cr} + \text{H} \rightarrow \text{H}^+ + \text{e}$	ζ
$\text{cr} + \text{H}_2 \rightarrow \text{H}_3^+ + \text{e} + \text{H} + \text{cr}$	2ζ
$\text{cr} + \text{He} \rightarrow \text{He}^+ + \text{e} + \text{cr}$	1.1ζ
Photoreactions [$\text{s}^{-1} \text{ molecule}^{-1}$]:	
$\gamma + \text{H}_2 \rightarrow 2 \text{H}$	$5.6 \times 10^{-11} \chi_{\text{FUV}} f_{\text{shield}}(N_{\text{H}_2}) e^{-3.74 A_V}$
$\gamma + \text{CO} \rightarrow \text{C} + \text{O}$	$2 \times 10^{-10} \chi_{\text{FUV}} f_{\text{shield}}(N_{\text{CO}}, N_{\text{H}_2}) e^{-3.53 A_V}$
$\gamma + \text{C} \rightarrow \text{C}^+ + \text{e}$	$3 \times 10^{-10} \chi_{\text{FUV}} e^{-3.4 A_V}$
$\gamma + \text{CH}_x \rightarrow \text{C} + \text{H}$	$1 \times 10^{-9} \chi_{\text{FUV}} e^{-1.5 A_V}$
$\gamma + \text{OH}_x \rightarrow \text{O} + \text{H}$	$5 \times 10^{-10} \chi_{\text{FUV}} e^{-1.7 A_V}$
$\gamma + \text{M} \rightarrow \text{M}^+ + \text{e}$	$3.4 \times 10^{-10} \chi_{\text{FUV}} e^{-1.9 A_V}$
$\gamma + \text{HCO}^+ \rightarrow \text{CO} + \text{H}$	$1.5 \times 10^{-10} \chi_{\text{FUV}} e^{-2.5 A_V}$
Ion–neutral reactions [$\text{cm}^3 \text{ s}^{-1} \text{ molecule}^{-1}$]:	
$\text{H}_3^+ + \text{CI} \rightarrow \text{CH}_x + \text{H}_2$	2×10^{-9}
$\text{H}_3^+ + \text{OI} \rightarrow \text{OH}_x + \text{H}_2$	8×10^{-10}
$\text{H}_3^+ + \text{CO} \rightarrow \text{HCO}^+ + \text{H}_2$	1.7×10^{-9}
$\text{He}^+ + \text{H}_2 \rightarrow \text{He} + \text{H} + \text{H}^+$	7×10^{-15}
$\text{He}^+ + \text{CO} \rightarrow \text{C}^+ + \text{O} + \text{H}$	$1.4 \times 10^{-9} / \sqrt{T/300}$
$\text{C}^+ + \text{H}_2 \rightarrow \text{CH}_x + \text{H}$	4×10^{-16}
$\text{C}^+ + \text{OH}_x \rightarrow \text{HCO}^+$	1×10^{-9}
Neutral–neutral reactions [$\text{cm}^3 \text{ s}^{-1} \text{ molecule}^{-1}$]:	
$\text{OI} + \text{CH}_x \rightarrow \text{CO} + \text{H}$	2×10^{-10}
$\text{CI} + \text{OH}_x \rightarrow \text{CO} + \text{H}$	$5 \times 10^{-12} \sqrt{T}$
Recombinations and charge transfers [$\text{cm}^3 \text{ s}^{-1} \text{ molecule}^{-1}$]:	
$\text{He}^+ + \text{e} \rightarrow \text{He} + \gamma$	$1 \times 10^{-11} / \sqrt{T} \times (11.19 - 1.676 \times \log_{10}(T) - 0.2852 \times \log_{10}(T^2) + 0.04433 \times \log_{10}(T^3))$
$\text{H}_3^+ + \text{e} \rightarrow \text{H}_2 + \text{H}$	$2.34 \times 10^{-8} (T/300)^{-0.52}$
$\text{H}_3^+ + \text{e} \rightarrow 3\text{H}$	$4.36 \times 10^{-8} (T/300)^{-0.52}$
$\text{C}^+ + \text{e} \rightarrow \text{CI} + \gamma$	$4.67 \times 10^{-12} (T/300)^{-0.6}$
$\text{HCO}^+ + \text{e} \rightarrow \text{CO} + \text{H}$	$2.76 \times 10^{-7} (T/300)^{-0.64}$
$\text{M}^+ + \text{e} \rightarrow \text{M} + \gamma$	$3.8 \times 10^{-10} T^{-0.65}$
$\text{H}_3^+ + \text{M} \rightarrow \text{M} + \gamma$	2×10^{-9}
Hydrogenic chemistry [$\text{cm}^3 \text{ s}^{-1} \text{ molecule}^{-1}$]:	
$\text{H}^+ + \text{e} \rightarrow \text{H}$	$2.753 \times 10^{-14} \times (315614/T)^{1.5} \times (1 + (115188/T)^{0.407})^{-2.242}$
$\text{H}_2 + \text{H} \rightarrow \text{H}$	$k_{\text{H},1} = 6.67 \times 10^{-12} \sqrt{T} \times e^{-\left(1.0 + \frac{63590}{T}\right)}$ $k_{\text{H},h} = 3.52 \times 10^{-9} e^{-\frac{43900}{T}}$ $n_{\text{cr,H}} = 10^{\left(3 - 0.416 \times \log_{10} T_4 - 0.327 \times (\log_{10}(T_4))^2\right)}$ $n_{\text{cr,H}_2} = 10^{\left(4.845 - 1.3 \times \log_{10}(T_4) + 1.62 \times (\log_{10}(T_4))^2\right)}$ $n_{\text{cr}} = (x_{\text{H}}/n_{\text{cr,H}} + x_{\text{H}_2}/n_{\text{cr,H}_2})^{-1}$ $\exp\left[(n/n_{\text{cr}})/(1.0 + n/n_{\text{cr}}) \times \log_{10}(k_{\text{H},h}) + 1/(1 + n/n_{\text{cr}}) \times \log_{10}(k_{\text{H},1})\right]$
$\text{H}_2 + \text{H}_2 \rightarrow \text{H}_2 + 2\text{H}$	$k_{\text{H}_2,1} = 5.996 \times 10^{-30} T^{4.1881} / (1 + 6.761 \times 10^{-6} \times T)^{(5.6881)} \times e^{-54.657.4/T}$ $k_{\text{H}_2,h} = 1.9 \times 10^{-9} \times e^{-53300/T}$ $\exp\left[(n/n_{\text{cr}})/(1.0 + (n/n_{\text{cr}})) \times \log_{10}(k_{\text{H}_2,h}) + 1/(1 + n/n_{\text{cr}}) \times \log_{10}(k_{\text{H}_2,1})\right]$
$\text{H} + \text{e} \rightarrow \text{H}^+ + 2\text{e}$	$\exp[-37.7 + 13.5 \times \ln(T_e) - 5.7 \times \ln(T_e)^2 + 1.6 \times \ln(T_e)^3 - 0.28 \times \ln(T_e)^4 + 0.03 \times \ln(T_e)^5 - 2.6 \times \ln(T_e)^6 + 1.1 \times \ln(T_e)^7 - 2.0 \times \ln(T_e)^8]$
$\text{He}^+ + \text{H}_2 \rightarrow \text{H}^+ + \text{He} + \text{H}$	$3.74 \times 10^{-14} e^{-35/T}$
$\text{H} + \text{H} + \text{grain} \rightarrow \text{H}_2 + \text{grain}$	$f_A = 1/(1 + 10^4 \times e^{-600/T_d})$ $3 \times 10^{-18} \sqrt{T} * f_A / (1 + 0.04 * \sqrt{T + T_d} + 0.002T + 8 \times 10^{-6} \times \sqrt{T})$
$\text{H}^+ + \text{e} + \text{grain} \rightarrow \text{H} + \text{grain}$	$\psi = \chi \sqrt{T} / n_e$ $12.25 \times 10^{-14} / \left(1 + 8 \times 10^{-6} \psi^{1.378} \left(1 + 508 \times T^{0.016} \psi^{-0.47 - 1.1 \times 10^{-5} \ln(T)}\right)\right)$

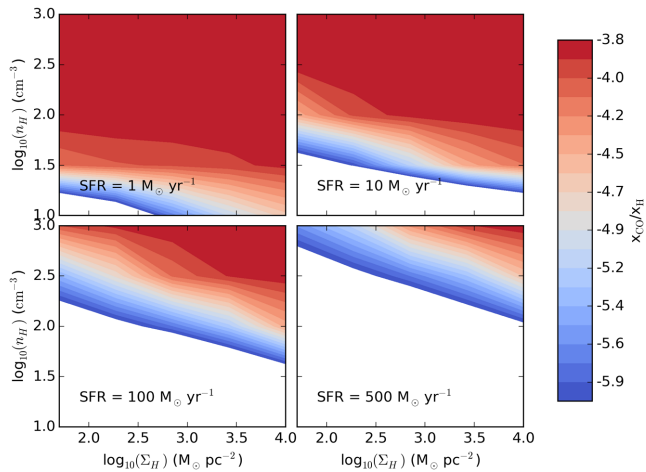


Figure 3. ^{12}CO abundance contours as a function of the volumetric and gas surface densities. Abundance contours are shown for four fiducial SFRs, which control the FUV flux and the cosmic ray ionization rates. At low radiation field strengths/cosmic ray ionization rates, nearly all of the carbon is in the form of CO. At higher SFRs, UV radiation and cosmic ray ionizations contribute to the destruction of CO, especially at low densities and surface densities. The whitespace in the contour subplots denotes abundances below $10^{-6}/\text{H}_2$.

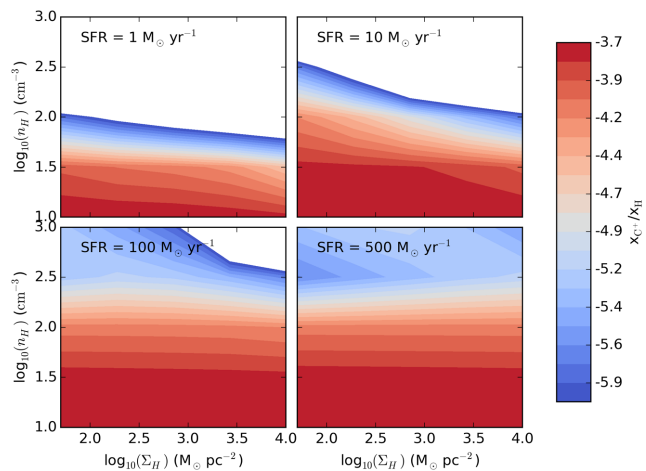


Figure 4. Similar to Fig. 3, but C⁺ abundance contours as a function of gas surface density and volumetric density. C⁺ abundances are increased in low volume density and surface density gas, and in high ultraviolet radiation fields and/or cosmic ray fluxes. The whitespace in the contour subplots denotes abundances below $10^{-6}/\text{H}_2$.

environments. In the remainder of this paper, we build upon this by combining this with our model for clouds in galaxies developed in Section 2.

3.2 Application to multiphase clouds

We are now in a place to understand the fractional abundances of carbon in its different phases in giant clouds. In Fig. 5, we present the radial fractional abundances for a variety of relevant species in our chemical reaction networks for three clouds of increasing surface density for a galaxy with gas mass $10^9 M_{\odot}$. These clouds are created within the context of the physical models developed in Sec-

tion 2.1, and therefore have increased SFRs (and UV fluxes/cosmic ray ionizations) with increasing cloud surface density.

For low surface density clouds, the hydrogen towards the outer most layers of the clouds is in atomic form. In these low surface density layers, photodissociation destroys H_2 , forming a PDR layer. At increasing cloud depths and surface densities, shielding by both gas and dust protects the gas from photodissociation, and hydrogen can transition from atomic to molecular phase via grain-assisted reactions.

The carbon chemistry follows a similar broad trend as the hydrogen chemistry – C⁺ dominates in the outer PDR layers of the cloud, and CO towards the inner shielded layers – though the chemistry is different. In particular, in addition to UV radiation, cosmic rays also contribute to the destruction of CO via the production of He^+ . As a result, for low volume density and surface density clouds, C⁺ can dominate the carbon budget both in the outer atomic PDR, as well as in much of the H_2 gas. Towards the cloud interior, the increased volume and surface densities within the cloud protect against the photodissociation/ionization of C I and CH_x/OH_x molecules (that are principal reactants in forming CO), as well as against the production of He^+ , which is a dominant destroyer of CO (Bisbas et al. 2015). Hence, in the innermost regions of clouds where the surface densities are highest, the carbon is principally in molecular CO form.

As the total column density of a cloud increases, the transition layer between atomic and molecular (both for hydrogen and carbon) is forced to shallower radii. This occurs because, although increasing column density raises the SFR and thus the UV and cosmic ray intensities, this is outweighed by the increase in cloud shielding and volume density that accompany a rise in Σ_g . The net effect is that clouds with high surface density and thus high SFR also tend to be dominated by CO, with only a small fraction of their carbon in the form of C⁺.

3.3 The [C II]–FIR relation

We are now in a position to compare our full model to the observed [C II]–FIR relation. We do so in Fig. 6, using a large range of galaxy gas masses in our model, chosen to be representative of the typical gas mass range of both local galaxies and high- z galaxies (Saintonge et al. 2011; Bothwell et al. 2013; Casey et al. 2014). We compare these model tracks to observational data from both low-redshift galaxies (grey points) and $z > 2$ galaxies (red triangles). We discuss the local deficit relation here, and defer discussion of the high- z data to Section 4.2. The local data are comprised of a compilation by Braucher, Dale & Helou (2008), as well as more recent $z \sim 0$ data taken by Díaz-Santos et al. (2013) and Farrah et al. (2013). Two trends are immediately evident from Fig. 6: (1) at fixed FIR luminosity, the [C II]/FIR ratio increases at larger galaxy gas mass, and (2) at increasing FIR luminosity, the [C II]/FIR ratio decreases for galaxies of a fixed gas mass. We discuss these trends in turn.

The trend with galaxy gas mass is straightforward to understand. The total SFR is an increasing function of both gas mass and gas surface density. Thus, an increase in gas mass at fixed SFR corresponds to a decrease in Σ_g . Because Σ_g is a primary variable controlling the chemical balance between C⁺ and CO, this in turn leads to an increase in the C⁺ abundance. The net effect is that, at fixed SFR (and hence FIR luminosity), higher gas mass galaxies have stronger [C II] emission.

The second broad trend, the decrease in the [C II]–FIR ratio with increasing FIR luminosity, is the so-called [C II]–FIR deficit. The origin of this is evident from examining the trends in both the gas

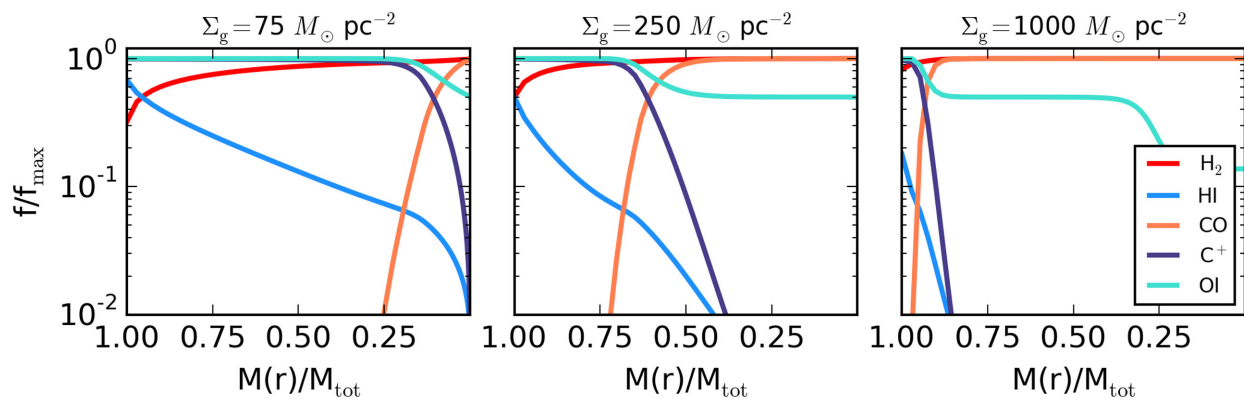


Figure 5. Radial variation of atomic and molecular abundances in three model clouds in a galaxy of $M_{\text{gal}} = 10^9 M_{\odot}$. The abundances are plotted against the Lagrangian mass enclosed such that a value of $M(r)/M_{\text{tot}} = 1$ corresponds to the surface of the cloud. Abundances are normalized to their maximum possible value, and plotted as a function of cloud radius. We show three clouds of increasing gas surface density. In general terms, the H_2 abundances increase towards the interior of clouds as shielding protects molecules from photodissociation. The carbon transitions from C^+ to CO, with the C^+ predominantly residing in the atomic PDRs and outer shell of H_2 gas. Clouds of increasing surface density have an increasing fraction of their gas in molecular H_2 form, and increasing fraction of their carbon locked in CO molecules. The oxygen abundances decrease towards the interior of clouds as the atom becomes locked up in CO and, in the inner parts of the highest surface density case, OH_x molecules.

physical properties and chemical abundances in the ISM calculated thus far (e.g. Fig. 5). C^+ dominates the weakly shielded PDR layers of giant clouds in the ISM, while CO principally resides in the well-shielded cloud interiors. Thus, an increase in Σ_g drives a decrease in the amount of C^+ and an increase in the amount of CO. At the same time, an increase in Σ_g drives an increase in SFR and thus in FIR luminosity. Thus, an increase in Σ_g leads to a sharp fall in the ratio of [C II]/FIR. In an actual sample of galaxies, the ratio of [C II] to FIR falls only shallowly with FIR, however, because the dependence on Σ_g is partly offset by the dependence on gas mass. That is, galaxies with higher FIR luminosities tend to have both higher gas surface densities and higher gas masses than galaxies with lower FIR luminosities. The former drives the [C II] luminosity down and the latter drives it up, but the surface density dependence is stronger (due to the exponential nature of FUV attenuation), leading to an overall net decrease in [C II] emission with FIR luminosity in the observed $z \sim 0$ sample.

4 DISCUSSION

4.1 Calorimetry of giant clouds

Nominally, [C II] line cooling is one of the principal coolants of the neutral ISM. Because the [C II] line emission does not increase in proportion to the SFR, it is interesting to consider where the cooling occurs in place of the [C II] line.

In Fig. 7, we revisit the cooling rates originally presented in Fig. 2. For clarity, we omit the heating rates, but additionally show the cooling rates from a subset of the individual CO and [O I] emission lines. As the cloud surface densities increase, the cooling rate of [C II] decreases dramatically. This owes principally to the plummeting C^+ abundances. At the same time, the dominant line cooling transitions to [O I] and CO. The increase in CO line cooling is in part due to the rapid increase in CO abundance as the increased cloud surface density protects the molecule from photodissociation, and increased volume density combats dissociation via He^+ . The CO cooling is dominated by mid- to high- J CO emission lines, with the power shifting to higher rotational transitions at higher gas surface densities (e.g. Narayanan & Krumholz 2014).

Alongside CO, line emission from [O I] is an important contributor at high cloud surface densities. To see why, consider again the radial abundances within a sample cloud presented in Fig. 5. Here, we now highlight the [O I] abundance gradients. While the fractional O I abundance decreases modestly with increasing gas surface density owing to increased molecule production (mostly CO and OH_x), O I remains relatively pervasive in both atomic and molecular gas. This is to be contrasted with ionized C^+ , which tends to reside principally in the atomic PDRs of clouds, and sometimes the outer layer of the H_2 core. So, while the mass fraction of H_2 to H I gas increases with increasing surface density clouds, [O I] remains an efficient coolant. The bulk of the cooling occurs via the [O I] $^3P_1 - ^3P_2$ transition, though emission from the $^3P_0 - ^3P_1$ [O I] line can be non-negligible at the highest gas surface densities.

We can also examine the ratio of [O I] to [C II] emission in our model, and compare that to observations. We do so in Fig. 8, using a compilation of data on luminous $z \sim 0.1$ – 0.3 galaxies from Graciá-Carpio et al. (2011) and Farrah et al. (2013), and low-luminosity local galaxies from Malhotra et al. (2001). We find that our fiducial model does a good job of reproducing the [O I]/[C II] ratios of luminous galaxies, but that it underpredicts the [O I] luminosities of low-FIR galaxies. We attribute this effect to the omission of a contribution from the diffuse ISM in our fiducial model, which likely dominates [O I] production in real low-luminosity galaxies; we show in Section 4.5.1 that including the diffuse component substantially ameliorates the disagreement.

Finally, it is worth discussing the relationship of CO observations to our model results. At first one might be tempted to compare the predicted line ratios shown in Fig. 7 to observations of the CO-to-[C II] $158 \mu\text{m}$ ratio in real galaxies (e.g. Mashian et al. 2015; Rosenberg et al. 2015). However, this requires more data than one might at first suspect. In our model, this line ratio is determined by the cloud surface density Σ_g , but the absolute luminosities of all lines, and the overall IR luminosity, are also linearly proportional to the total gas mass. Because the surface density is not known for the real galaxies, only the absolute line fluxes and luminosity, one can essentially always fit the observations by choosing a value of Σ_g that produces the desired CO/[C II] line ratio, and then choosing a total gas mass to match the required infrared

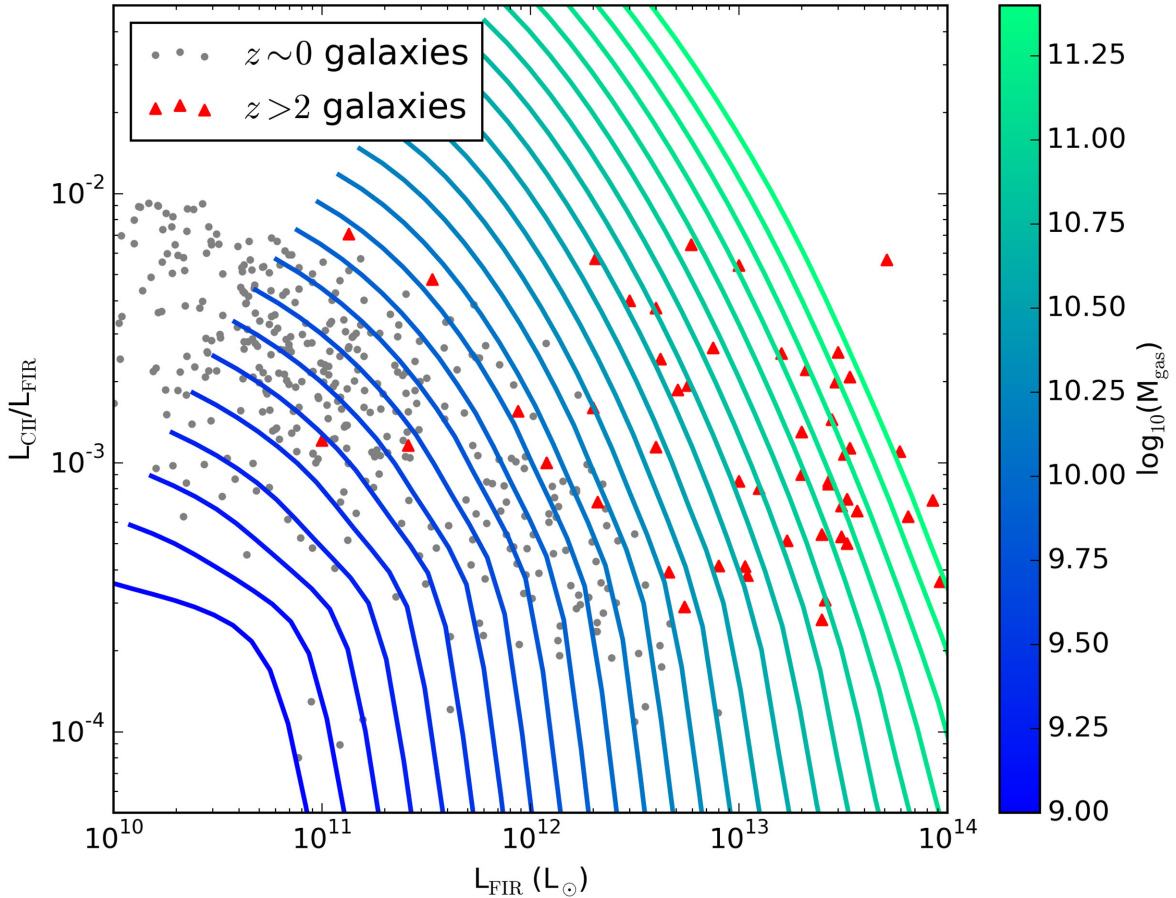


Figure 6. Theoretical [C II] luminosities (normalized by the FIR luminosity) as a function of FIR luminosity. The model tracks show predictions for galaxy gas masses $\log_{10}(M_{\text{gal}}) = [9, 11.3]$. Increasing L_{FIR} for a given galaxy corresponds to increasing Σ_{g} for the clouds it contains, and with values bracketed by the range we explore $\Sigma_{\text{g}} = 50\text{--}5000 M_{\odot} \text{pc}^{-2}$. The grey points show local $z \sim 0$ data, and the red triangles show high- z data. The lowest mass model track corresponds to the leftmost one. The [C II]–FIR deficit in galaxies owes principally to a decrease in PDR mass in galaxies with increasing infrared luminosity. High-redshift galaxies are observed to be systematically at a higher infrared luminosity at a given [C II]/FIR luminosity ratio as compared to low- z galaxies. In our model, this arises because galaxies at high- z have systematically larger gas masses. At a fixed SFR, an increased gas mass means lower cloud surface densities on average, which results in higher [C II] luminosities. High- z detections are from Cox et al. (2011), De Breuck et al. (2011), George et al. (2013), Graciá-Carpio et al. (2011), Ivison et al. (2010), Maiolino et al. (2005), Rawle et al. (2013), Stacey et al. (2010), Swinbank et al. (2012), Valtchanov et al. (2011), Venemans et al. (2012), Wagg et al. (2012), Wang et al. (2013), Willott, Omont & Bergeron (2013), Díaz-Santos et al. (2016), Schaerer et al. (2015) and Gullberg et al. (2015).

luminosity. In effect, a comparison of our model’s predictions of L_{IR} with $L_{\text{CO}}/L_{\text{CII}}$ is an attempt to fit two observed quantities using a model with two free parameters (Σ_{g} and M_{gal}), which is not particularly illuminating.

However, we can make a meaningful comparison to galaxies in which L_{CO} , L_{CII} and L_{FIR} have all been measured independently. In this three-dimensional space, our models and its two free parameters define a two-dimensional surface, and we can investigate how close observations lie to the predicted surface. The measurement of L_{CO} requires particular care, because the natural comparison with our models is the full CO luminosity integrated over all lines. In the literature, we culled two samples: the first is from Mashian et al. (2015), who measures the CO Spectral Line Energy Distribution from the $J=4\text{--}3$ through $J=13\text{--}12$ lines. We assume that the remainder of the missing power comes from the CO ($J=3\text{--}2$) line that does not have reported luminosities in the Rosenberg et al. (2015) work, and that the CO ($J=3\text{--}2$) line has the same luminosity in each system as the CO ($J=4\text{--}3$) line. The [C II] and FIR luminosities for the Rosenberg et al. (2015) sample are reported in the same paper. The second sample is hand-picked from the Narayanan

& Krumholz (2014) theoretical study of CO SLEDs, and includes NGC 253, M82, NGC 6240 and the Eyalash. For the latter four galaxies, for any missing CO transitions we utilize the fitting functions of Narayanan & Krumholz (2014) to fill in the missing data. For this latter sample, the C II and FIR observational data we use are taken from Brauer et al. (2008), Ivison et al. (2010), Sanders et al. (2003) and Díaz-Santos et al. (2013).

We compare these galaxies to our models in Fig. 9. For our model predictions, we construct the $L_{\text{CO}}\text{--}L_{\text{CII}}\text{--}L_{\text{FIR}}$ surface via a Delaunay triangulation of the $(L_{\text{CO}}, L_{\text{CII}}, L_{\text{CO}})$ coordinates that result from evaluating our models on our grid of points in Σ_{g} and M_{gal} . In the first two panels of Fig. 9, we compare the observations to the predicted model surface. To make the comparison more quantitative, we also compute the 3D distance between each observed galaxy and the closest point on our theoretical model surface in the space of $(\log L_{\text{CO}}, \log L_{\text{CII}}, \log L_{\text{CO}})$. The resulting distance in dex characterizes how close the observations come to our predicted locus. The comparison between the model and data shows reasonable agreement. The distance from the $L_{\text{CO}}\text{--}L_{\text{CII}}\text{--}L_{\text{FIR}}$ plane ranges from ~ 0.01 to 1 dex.

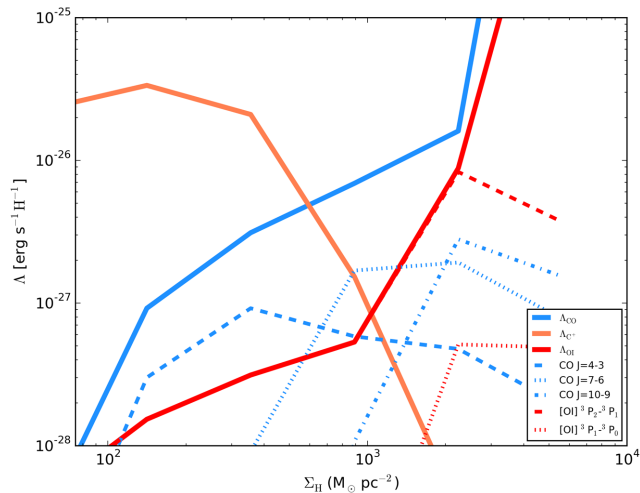


Figure 7. Cooling rates of individual lines as a function of cloud surface density for a model galaxy of mass $M_{\text{gal}} = 10^9 M_{\odot}$. As the [C II] luminosities decrease with increasing gas surface density, the principal cooling transitions to CO and [O I] emission lines. At high surface densities, the CO cooling is dominated by high- J rotational transitions. Note that, because we only show a subset of the CO lines for clarity, the sum of the cooling rates of the shown CO lines will not add up to the total CO cooling rate shown.

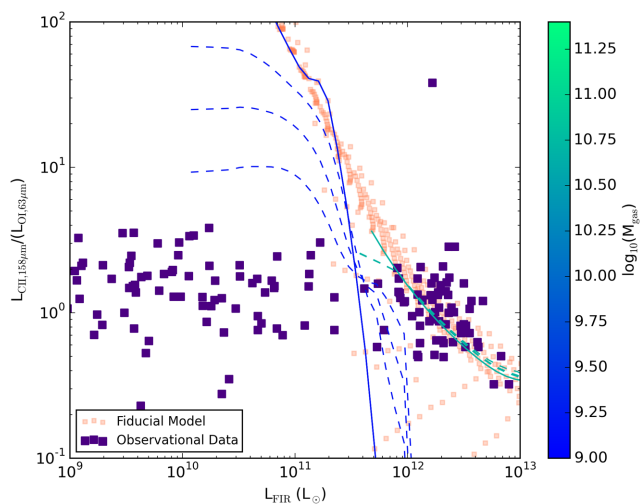


Figure 8. [C II]/[O I] luminosity ratios for model compared to data from Graciá-Carpio et al. (2011), Farrah et al. (2013) and Malhotra et al. (2001). The orange squares show all galaxies in our fiducial model, while the purple squares show observational data. The lines show individual tracks for a low ($M_{\text{gal}} \sim 10^9 M_{\odot}$; blue) and high ($M_{\text{gal}} \sim 10^{11} M_{\odot}$; green) gas mass galaxy. The solid lines show our fiducial model (hence, they go through a subset of the orange squares), while the dashed lines show the effect of including a diffuse neutral ISM component that comprises 0.25, 0.5 and 0.75 the total neutral gas mass budget. The 25 per cent lines are the ones closest to the solid lines, and the diffuse ISM contribution to the total mass budget increases as the dashed lines are further removed from the solid lines. For low-luminosity galaxies, a substantial contribution to the O I luminosity from diffuse neutral gas is required to match the observations. See Section 4.5.1 for details. For both the observations and the models, we take the [O I] luminosity to be just the $63 \mu\text{m}$ line as this always dominates over the $145 \mu\text{m}$ line.

4.2 Application to high-redshift galaxies

Recent years have seen a large increase in the number of [C II] detections from heavily star-forming galaxies at $z \gtrsim 2$ (e.g. Hailey-Dunsheath et al. 2008; Stacey et al. 2010; Brisbin et al. 2015; Gullberg et al. 2015; Schaerer et al. 2015), extending to the epoch of reionization (e.g. Riechers et al. 2013; Wang et al. 2013; Rawle et al. 2014; Capak et al. 2015). Returning to Fig. 6, we now highlight the high-redshift compilation denoted by the red triangles. The compilation is principally culled from the Casey et al. (2014) review article, with some more recent detections. We exclude data that have upper limits on either [C II] or FIR emission. It is clear that the high- z data are offset from low- z galaxies such that at a fixed [C II]/FIR luminosity ratio, $z \sim 2$ –6 galaxies have a larger infrared luminosity. One possible interpretation of the high- z data is that the high- z galaxies exhibit a [C II]–FIR deficit akin to that observed in local galaxies, but shifted to higher luminosities.

We now highlight the model tracks overlaid for galaxies of mass between $M_{\text{gal}} = 10^{10}$ and $10^{11.3} M_{\odot}$. These gas masses are chosen based on the range of H_2 gas masses constrained for a sample of high- z submillimetre galaxies by Bothwell et al. (2013). As is evident from Fig. 6, the model tracks for galaxies with large gas mass show good correspondence with the observed high- z data points. This suggests that the ultimate reason for the offset in infrared luminosity for the [C II]–FIR deficit of high- z galaxies is their large gas masses. High infrared luminosity galaxies at $z \sim 0$ typically have high SFRs due to large values of Σ_{g} , but those at high- z have high SFRs due to large gas masses instead.

Our interpretation for the offset in infrared luminosity in the high- z [C II]–FIR deficit is consistent with a growing body of evidence that, at a fixed stellar mass, galaxies at high redshift have higher SFRs and gas masses than those at $z \sim 0$ (Davé et al. 2010; Narayanan et al. 2010, 2015; Geach et al. 2011; Rodighiero et al. 2011; Narayanan, Bothwell & Davé 2012b; Madau & Dickinson 2014), and that it is these elevated gas masses that are driving the extreme SFRs, rather than a short-lived starburst event. As an example, the most infrared-luminous galaxies at $z \sim 0$ have small emitting areas (~ 1 kpc), and large measured gas surface densities, up to $\sim 10^3 M_{\odot} \text{pc}^{-2}$ averaged over the emitting area. In contrast, galaxies of comparable luminosity at high- z have a diverse range of sizes, with some gas spatial extents observed ~ 20 kpc (Ivison et al. 2011; Casey et al. 2014; Spilker et al. 2014; Dunlop et al. 2016; Rujopakarn et al. 2016). Indeed, cosmological zoom simulations have shown that the extreme SFRs of the most infrared-luminous galaxies $L_{\text{IR}} \sim 10^{13} L_{\odot}$ at $z \sim 2$ can be driven principally by significant reservoirs of extended gas at a moderate surface density (Narayanan et al. 2015; Feldmann et al. 2016; Geach et al. 2016). Similarly, at lower luminosities at $z \sim 2$, Elbaz et al. (2011) find that the cold dust Spectral Energy Distributions of main-sequence galaxies are consistent with more extended star formation at lower surface densities than their low- z counterparts. Our model suggests that the offset in the [C II]–FIR relation between $z \sim 0$ and $z \sim 2$ galaxies can ultimately be traced to the same phenomenon.

4.3 Relationship to other theoretical models

There has been significant attention paid to modelling [C II] emission from galaxies over the past 5–10 years. The methods are broad, and range from numerical models of clouds, as in this paper, to semi-analytic dark matter only simulations to full cosmological hydrodynamic calculations. Generally, models have fallen into three camps (with some overlap): (1) models that study the

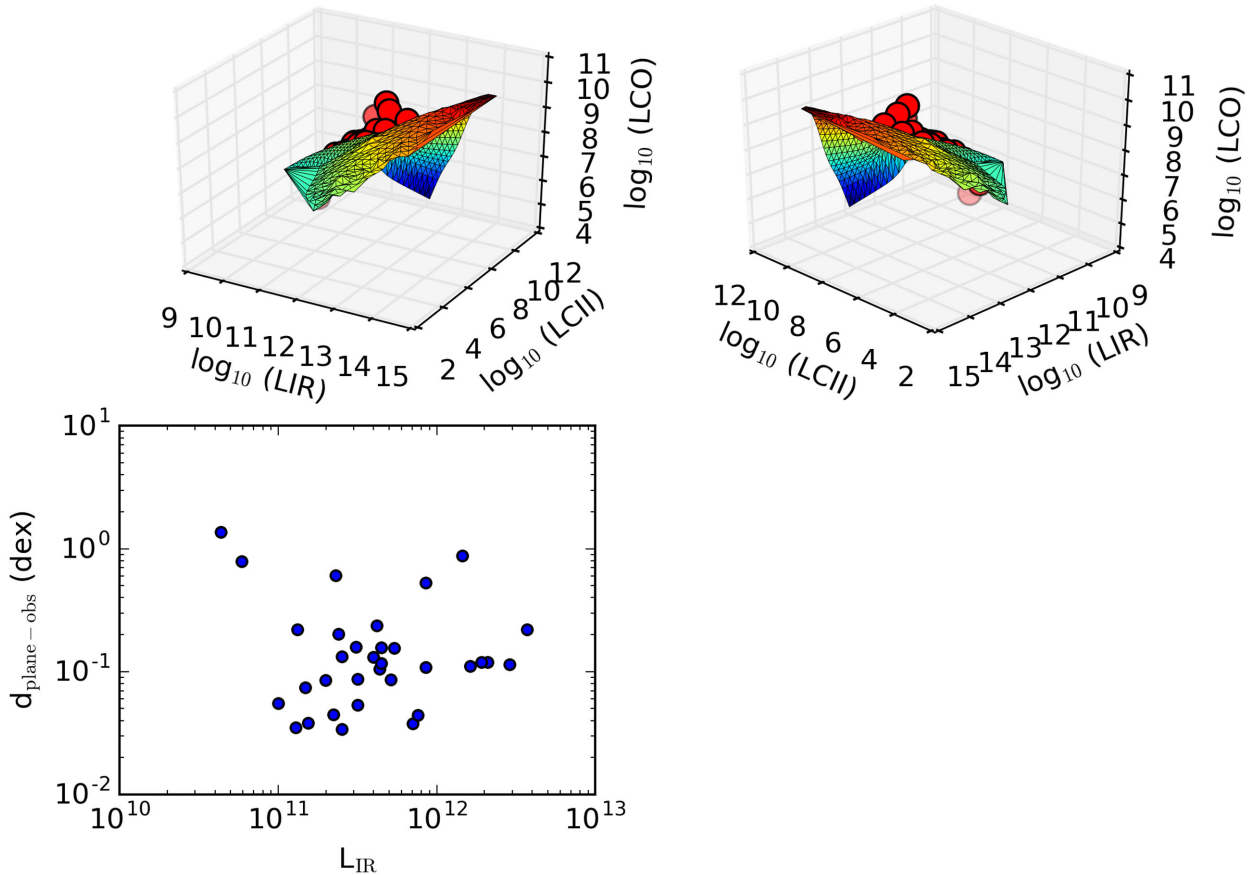


Figure 9. Top left and top right: theoretical L_{CO} - L_{CII} - L_{FIR} surface compared to observations. The top left and top right are the same plot from two different viewing angles. The luminosities are all in L_{\odot} . The surface is the loci of possible L_{CO} - L_{CII} - L_{FIR} points produced by our models as we vary Σ_g and M_{gal} , while the red circles indicate observations. The CO luminosities shown and the integrated luminosity are over all transitions. See the text for details of this calculation. Bottom left: distance from theoretical L_{CO} - L_{CII} - L_{FIR} surface and the observations (measured in dex) as a function of L_{FIR} .

[C II]-SFR relationship in low-luminosity galaxies at a given redshift (e.g. Olsen et al. 2015); (2) models predicting [C II] emission from epoch of reionization galaxies (Nagamine, Wolfe & Hernquist 2006; Muñoz & Furlanetto 2013a,b; Vallini et al. 2013, 2015; Pallottini et al. 2015); and (3) models that aim to understand the [C II]-FIR deficit in luminous galaxies. We focus on comparing to other theoretical models in this last category as they pertain most directly to the presented work here.

Abel et al. (2009) use CLOUDY H II region models (Ferland et al. 2013) to explore the idea, first posited by Luhman et al. (2003), that [C II] emission is suppressed in high-SFR galaxies because H II regions become dust bounded rather than ionization bounded. In their model, this reduces the [C II] luminosity because ionizing photons absorbed by dust are not available to ionize carbon. Following on this work, Fischer et al. (2014) utilized CLOUDY models to present comparisons between both fine structure line luminosities and FIR colours, as well as fine structure line luminosities and molecular absorption features. While modelling molecular absorption lines is outside the scope of this work, in Fig. 10, we show the relationship between the FIR dust colours (parametrized by the 60/100 μm ratio) and the [C II]/FIR and [C II]/[O I] luminosity ratios. We calculate the dust colours by assuming that the dust constitutes an optically thin grey body with a source function

$$S(\nu) = \frac{\nu^{\beta+3}}{e^{h\nu/kT} - 1}. \quad (17)$$

We adopt a dust spectral index $\beta = 2$, but our results are not terribly sensitive to this choice [though note that equation (17) assumes optically thin emission, which may not be the case at the centres of starbursts]. We find very good correspondence between the locus of model points and the observed data from Malhotra et al. (2001). The fact that there are model results that do not fall within the range of observed data is simply a statement that our explored parameter space includes some models that may be unrepresentative of real galaxies (for example extremely luminous but low surface density galaxies).

Bisbas et al. (2015) developed cloud models with similar underlying methods to those presented here, based on the 3D-PDR code. They use their models to investigate the chemistry of CO, and find, as we do, that at high SFRs He^+ destruction of CO becomes an important process in determining the overall carbon chemical balance in a galaxy. However, they do not consider [C II] emission or its relationship with SFRs. Similarly, Popping et al. (2014) developed semi-analytic galaxy formation models coupled with PDR modelling to model CO, C I and [C II] emission from model galaxies. The models provide a reasonable match to the observed $z \sim 0$ [C II]-FIR deficit, but the authors do not discuss the physical origin of the effect, nor its redshift dependence.

Muñoz & Oh (2015) posited an analytic model in which [C II] line saturation may drive the observed [C II]/FIR luminosity deficit. At very high temperatures ($T_{\text{gas}} \gg T_{\text{[CII]}}$), the line luminosity no longer increases with temperature, and they suggest that this

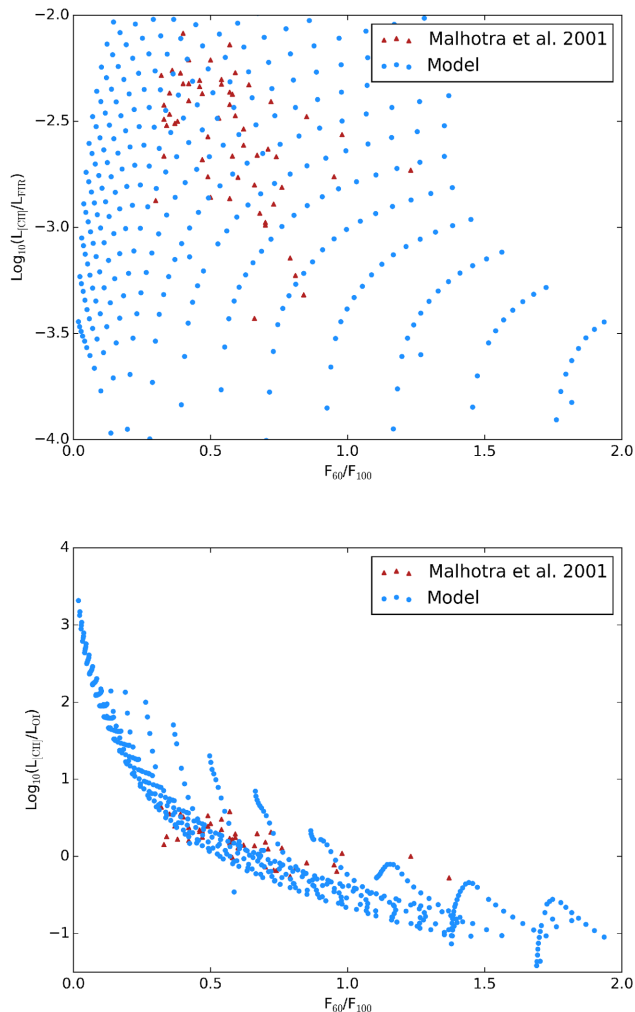


Figure 10. [C II]/FIR luminosity ratio versus infrared colour, as well as [C II]/[O I] luminosity ratio versus infrared colour. Blue circles represent our model while red triangles denote *ISO* data from Malhotra et al. (2001). The fact that the observed data in the top panel only occupy a narrow range of the theoretical points likely owes to regions in the M_{gal} , Σ_{g} parameter space covered by our models that are unrepresentative of real galaxies.

phenomenon is why [C II] stops increasing with SFR at high SFRs. However, our models suggest that the gas temperatures typically do not reach such high values, at least up to $L_{\text{FIR}} \sim 10^{13}$. For example, turning to Fig. 2, we find maximum⁶ gas temperatures of ~ 50 K at luminosities of $L_{\text{FIR}} = 10^{13} L_{\odot}$. Further bolstering this claim, Narayanan et al. (2011b) ran idealized hydrodynamic galaxy merger simulations with thermal balance models similar to the ones presented in this paper, though with the increased sophistication of directly modelling the dust temperature via 3D dust radiative transfer calculations. Narayanan et al. (2011b) found that even for clouds in merger-driven starbursts that exceed $\Sigma_{\text{H}_2} > 10^4 M_{\odot} \text{pc}^{-2}$, the gas kinetic temperature remained $T_{\text{kin}} \sim 10^2$ K. Thus, within the context of the thermal balance equations presented in this work, we conclude that line saturation is not likely to dominate the [C II]/FIR luminosity deficit at high infrared luminosities.

⁶ This number of course increases with increasing galaxy gas mass. Functionally, we find a maximum temperature of $T \sim 100$ K for our most massive galaxies.

Finally, while it was not intended to specifically address the [C II]–FIR deficit in galaxies (indeed the phenomenon had not yet been observed), it is worth highlighting the PDR models of Wolfire, Hollenbach & Tielens (1989). These models found that as PDR densities increase, the size of the [C II] emitting region decreases, causing a drop in the [C II]/FIR luminosity ratio. Our models agree with these calculations, though also find that cloud surface density plays an important role in setting the chemical equilibrium.

4.4 Relationship to observations

There are a few observational works in recent years that discuss particular aspects of the [C II]/FIR luminosity deficit with FIR luminosity that are worth discussing within the context of the model that we present in this paper. In early work, Stacey et al. (1991) utilized PDR models to interpret their KAO observations of a sample of nearby gas-rich galaxies. These authors found that single-component PDR models did not fit their observed [C II]/FIR luminosity ratios, and posited a two-component model in which the bulk of the FIR emission arises from a confined region exposed to a high-intensity UV field, while the [C II] line emission mostly comes from a more diffuse extended component exposed to a lower radiation field. This is compatible with the model we present here. While in our model we assume for simplicity that a given galaxy is comprised of a single population of clouds, in reality a galaxy will have a distribution of cloud surface densities, likely with the high- Σ_{g} clouds towards the central regions associated with more active star formation. In this scenario, the FIR luminosity would predominantly arise from the high- Σ_{g} clouds, while the lower Σ_{g} clouds would produce more [C II] line emission, consistent with the model developed by Stacey et al. (1991).

Díaz-Santos et al. (2013) presented *Herschel* observations of 241 nearby galaxies, and confirmed the [C II]–FIR deficit in their relatively large sample. They find that the LIRGs with higher infrared luminosity surface density tend to have lower [C II]/FIR luminosity ratios compared to more extended systems. Similar results have been found for some high- z dusty galaxies by Spilker et al. (2016). Within the context of our model, we interpret this result as higher infrared luminosity density galaxies corresponding to higher gas surface density galaxies (Kennicutt & Evans 2012). Galaxies with higher gas surface densities will have lower atomic PDR masses with respect to their H_2 molecular masses, and therefore lower [C II] luminosities. Of course, it is important to note that galaxy-averaged measurements such as those in Díaz-Santos et al. (2013) will not correspond exactly to our simulations. Our models are of individual clouds, while beam-averaged measurements of galaxies measure the aggregate properties of numerous clouds with different individual properties. Even if all clouds in a galaxy had identical properties (as in our model), the results from our model as compared to observed galaxies would differ by the typical cloud filling factor in galaxies.

4.5 Uncertainties in the model

While we aim to provide a relatively minimalist analytic model for the structure of giant clouds in galaxies in Section 2, there are a number of uncertainties and simplifications that can impact the output of our models. In this section, we explore the impact of these parameters on our results.

4.5.1 Contribution from the diffuse ISM

In order to model luminous systems, we have assumed that the bulk of the atomic line-emitting gas in galaxies is confined to the PDR regions that bound giant clouds. While this approximation is reasonable for LIRGs and ULIRGs, where the ISM is known to be dominated by molecular gas, it becomes increasingly questionable if applied to galaxies with SFRs comparable to or smaller than that of the Milky Way. These galaxies have ISM where the mass is dominated by diffuse warm H I, while the molecular and cold atomic components are subdominant. Since our focus in this paper is on more luminous galaxies, for the bulk of the paper we have ignored this issue, but in this section we consider the potential impact of a diffuse component on our results.

For simplicity, we model the diffuse component as a one-zone DESPOTIC cloud model with fiducial physical properties $N_{\text{H}} = 1 \times 10^{20} \text{ cm}^{-2}$ and $n_{\text{H}} = 0.1 \text{ cm}^{-3}$, typical of the warm atomic medium in the Milky Way. We consider four possibilities: that the diffuse component occupies a mass fraction 0, 0.25, 0.5 and 0.75 of the total mass budget; the choice 0 corresponds to the fiducial model we have used elsewhere in this paper.

In Fig. 8, we plot the $[\text{C II}]/[\text{O I}]$ ($63 \mu\text{m}$) luminosity ratio as a function of FIR luminosity for two model galaxies representing both low and high gas masses ($\sim 10^9$ and $10^{11} M_{\odot}$). The dashed lines denote different diffuse gas mass fractions, and the solid lines show our fiducial model (with no diffuse gas). Therefore, the lowest diffuse gas fractions (0.25) are the lines closest to the solid line, and successive lines show increasing diffuse gas mass fractional contributions (0.5 and 0.75).

In low-mass galaxies, a neutral diffuse ISM component can contribute to both $[\text{C II}]$ and $[\text{O I}]$ line emission. Not surprisingly, the diffuse component contribution is maximized in our 75 per cent diffuse model, and for the case of a small total gas mass, corresponding to low SFR and thus a low FUV radiation field in the galaxy. In this limiting case, there is relatively little atomic gas if we do not explicitly include a diffuse component, and putting one in increases the $[\text{C II}]$ luminosity by a factor of a few compared to a model with the same ISM mass but no diffuse component. However, this component makes a much larger contribution to the $[\text{O I}]$ luminosity, increasing it by more than an order of magnitude. The difference comes from the temperature sensitivities of the lines: the excited state responsible for $[\text{C II}]$ emission requires only 91 K to excite, and thus is readily produced even in the cool atomic envelopes of molecular clouds. In contrast, the $[\text{O I}]$ $63 \mu\text{m}$ line is produced by a level that is 228 K above ground. In models where our total gas mass and thus SFRs are small, the envelopes of giant clouds tend to be much cooler than this, and thus produce relatively little $[\text{O I}]$. The addition of a substantially warmer atomic component to the model therefore greatly increases the predicted $[\text{O I}]$ luminosity. In contrast, at higher gas masses and SFRs, as we approach the LIRG and ULIRG regime, the atomic envelopes are warm enough to produce $[\text{O I}]$. Thus, the effect of the diffuse component on the total $[\text{O I}]$ luminosity is smaller, and the effect on the $[\text{C II}]$ luminosity is smaller still.

Comparing models including a diffuse component to the observations of low-luminosity galaxies from Malhotra et al. (2001) shown in Fig. 8, we find that our models without a diffuse neutral ISM are unable to match the observed low $[\text{C II}]/[\text{O I}]$ luminosity ratios, but that addition of a diffuse component brings the models much closer to the data. Even our model with 75 per cent diffuse gas mass is unable to fully match the low observed $[\text{C II}]/[\text{O I}]$ luminosity ratios in low-luminosity galaxies. However, this may simply be because we

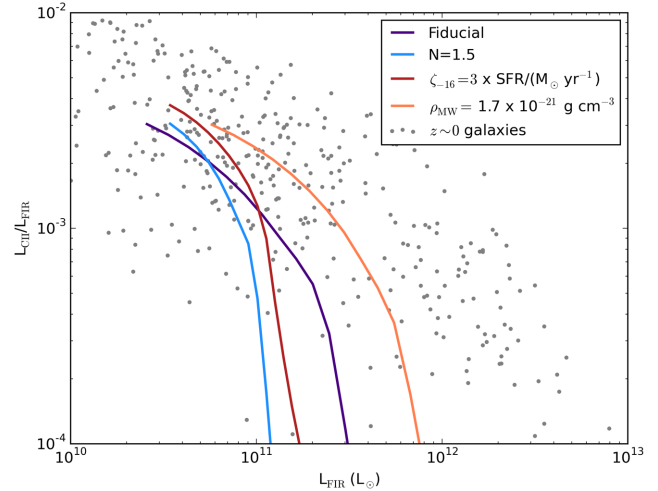


Figure 11. $[\text{C II}]/\text{FIR}$ luminosity ratio versus FIR luminosity for our fiducial model (thick blue), and three varying parameters in our cloud models. The example shown is for an $M_{\text{gal}} = 3 \times 10^9 M_{\odot}$ galaxy, the average mass (in log space) of our low-redshift galaxy mass range. See Table 1 for variable definitions.

have not considered even larger diffuse gas fractions [which would be eminently justified observationally for galaxies less luminous than the Milky Way – e.g. Bolatto et al. (2011) find an H I mass fraction of 95 per cent for the Small Magellanic Cloud], because we have simplistically treated the diffuse ISM as a single component with a single density and column density, or because we have not considered the effects of sub-solar metallicity, which will tend to make the ISM warmer and thereby increase the $[\text{O I}]/[\text{C II}]$ ratio. Since the focus of this study is on high-luminosity, heavily star-forming systems, and for such galaxies the inclusion of a diffuse ISM component has a negligible effect, we have not attempted to further refine our models to match the low-luminosity data.

4.5.2 Star formation law and cosmic rays

In the remainder of this section, we investigate the impact of our assumed parameter choices in modelling star-forming giant clouds in galaxies. In Fig. 11, we summarize the impact of varying the star formation law index (N), the density normalization (ρ_{MW}) and the cosmic ray ionization rate (ζ_{-16}).

All of these values are uncertain. Star formation indices ranging from sublinear to quadratic have been reported in the literature (Kennicutt & Evans 2012). Decreasing the star formation law index decreases the average density of our model clouds, which has a twofold effect. First, it decreases the total SFR via longer cloud free-fall times. Secondly, $[\text{C II}]$ is more easily formed owing to decreased recombination and molecular formation rates. Increasing the cloud density normalization (ρ_{MW}) has the opposite effect.

Similarly, the cosmic ray ionization rate in galaxies is uncertain. Observations of H_3^+ within the Galaxy suggest rates that range from $\zeta_{-16} \approx 0.1$ to 3 (McCall et al. 1999; Indriolo et al. 2007; Neufeld et al. 2010; Wolfire, Hollenbach & McKee 2010). For lack of a better constraint, we have chosen to employ a relatively conservative value, $\zeta_{-16} = 0.1 \times \text{SFR}/(M_{\odot} \text{ yr}^{-1})$, noting that increased cosmic ray ionization rates tend to result in more $[\text{C II}]$ flux. This is shown explicitly in Fig. 11, where we test a model with $\zeta_{-16} = 3 \times \text{SFR}/(M_{\odot} \text{ yr}^{-1})$.

For all of these tested variations in our parameter choice survey, the overall trend is similar: the [C II]/FIR luminosity ratio decreases with increasing galaxy SFR. This is because the net decrease in the [C II]/FIR luminosity ratio owes to decreasing relative PDR masses in increasingly luminous galaxies in our model. The normalization and exact behaviour of course depend on uncertain parameters, but the broad trends are robust.

Finally, we note that the linear scaling of the cosmic ray ionization rate with SFR is rooted in the tentative observational evidence for such a scaling by Abdo et al. (2010) and González-Alfonso et al. (2013). However, it is plausible that the cosmic ray ionization rate scales with some other parameter, such as SFR density or surface density. We defer a more thorough investigation into the chemical consequences of varying ionization rate scalings to a forthcoming study.

5 SUMMARY

We have developed models for the physical structure of star-forming giant clouds in galaxies, in which clouds consist of both atomic and molecular hydrogen. We coupled these cloud models with chemical equilibrium networks and radiative transfer models in order to derive the radial chemical and thermal properties, and utilized these models to investigate the origin of the [C II]/FIR luminosity deficit in luminous galaxies. Our main results are as follows.

(i) The carbon-based chemistry in clouds can be reduced to a competition between volumetric density and surface density protecting the formation of molecules against cosmic ray-induced ionizations and UV photodissociations/ionizations.

(ii) At solar metallicities, the molecular H₂ core in clouds tends to be well shielded from UV radiation, and dense enough to combat CO destruction by cosmic rays (via an intermediary He⁺ reaction) as well as ultraviolet radiation. As a result, the carbon in molecular gas is principally in the form of CO. This said, the lower surface density surfaces of the central molecular core can contain significant amounts of C⁺.

(iii) The opposite is true for atomic PDRs. The carbon in the PDR shell in clouds is easily exposed to the radiation and cosmic ray field, resulting in the bulk of carbon being in ionized C⁺ form.

(iv) At increasing galaxy SFR (and infrared luminosity), the typical cloud surface density (Σ_g) rises; with increasing Σ_g , the molecular fraction (H₂/H I) rises, and the relative [C II] luminosity decreases owing to a shrinking of the size of the [C II] emitting region. These reduced PDR masses in increasingly luminous galaxies are the fundamental origin of the [C II]/FIR luminosity deficit with FIR luminosity in galaxies in our model.

(v) As the [C II] luminosity decreases in high surface density clouds, the major coolants of the ISM transition to high-*J* CO emission lines and [O I].

(vi) At a fixed SFR, galaxies of increasing gas mass have lower cloud surface densities, and hence larger [C II] luminosities. Because of this, galaxies at high redshift, which have larger gas fractions than their low-*z* counterparts, lie offset from low-*z* galaxies in [C II]–FIR space. Our model provides a natural explanation for the offset [C II]–FIR deficit for high-*z* galaxies.

ACKNOWLEDGEMENTS

The authors thank Thomas Bisbas, Tanio Diaz-Santos, Duncan Farrah, Munan Gong, Javier Gracia-Carpio and Eve Ostriker for providing both simulation and observational data that aided us when

developing these models. DN thanks Aaron Evans, Thomas Greve, Rob Kennicutt, Dominik Riechers, J. D. Smith, Gordon Stacey, Dan Stark, Karen Olsen and Mark Wolfire for helpful conversations. Partial support for DN was provided by NSF AST-1009452, AST-1445357, NASA HST AR-13906.001 from the Space Telescope Science Institute, which is operated by the Association of University for Research in Astronomy, Incorporated, under NASA Contract NAS5-26555, and a Cottrell College Science Award, awarded by the Research Corporation for Science Advancement. MRK acknowledges support from US NSF grant AST-1405962 and Australian Research Council grant DP160100695.

REFERENCES

- Abdo A. A. et al., 2010, *ApJ*, 709, L152
 Abel N. P., Dudley C., Fischer J., Satyapal S., van Hoof P. A. M., 2009, *ApJ*, 701, 1147
 Abrahamsson E., Krems R. V., Dalgarno A., 2007, *ApJ*, 654, 1171
 Barinova G., van Hemert M. C., Krems R., Dalgarno A., 2005, *ApJ*, 620, 537
 Beirão P. et al., 2010, *A&A*, 518, L60
 Bertoldi F., McKee C. F., 1992, *ApJ*, 395, 140
 Bigiel F., Leroy A., Walter F., Brinks E., de Blok W. J. G., Madore B., Thornley M. D., 2008, *AJ*, 136, 2846
 Bisbas T. G., Papadopoulos P. P., Viti S., 2015, *ApJ*, 803, 37
 Blanc G. A., Heiderman A., Gebhardt K., Evans N. J., II, Adams J., 2009, *ApJ*, 704, 842
 Bolatto A. D., Leroy A. K., Rosolowsky E., Walter F., Blitz L., 2008, *ApJ*, 686, 948
 Bolatto A. D. et al., 2011, *ApJ*, 741, 12
 Boselli A., Lequeux J., Gavazzi G., 2002, *Ap&SS*, 281, 127
 Bothwell M. S. et al., 2013, *MNRAS*, 429, 3047
 Brauer J. R., Dale D. A., Helou G., 2008, *ApJS*, 178, 280
 Brisbin D., Ferkinhoff C., Nikola T., Parshley S., Stacey G. J., Spoon H., Hailey-Dunsheath S., Verma A., 2015, *ApJ*, 799, 13
 Capak P. L. et al., 2015, *Nature*, 522, 455
 Casey C. M., Narayanan D., Cooray A., 2014, *Phys. Rep.*, 541, 45
 Chomiuk L., Povich M. S., 2011, *AJ*, 142, 197
 Cox P. et al., 2011, *ApJ*, 740, 63
 Croxall K. V. et al., 2012, *ApJ*, 747, 81
 Daddi E. et al., 2010, *ApJ*, 713, 686
 Davé R., Finlator K., Oppenheimer B. D., Fardal M., Katz N., Kereš D., Weinberg D. H., 2010, *MNRAS*, 404, 1355
 De Breuck C., Maiolino R., Caselli P., Coppin K., Hailey-Dunsheath S., Nagao T., 2011, *A&A*, 530, L8
 de Looze I., Baes M., Bendo G. J., Cortese L., Fritz J., 2011, *MNRAS*, 416, 2712
 Díaz-Santos T. et al., 2013, *ApJ*, 774, 68
 Diaz-Santos T. et al., 2016, *ApJ*, 816, L6
 Dobbs C. L., Burkert A., Pringle J. E., 2011, *MNRAS*, 413, 2935
 Dobbs C. L. et al., 2013, in Beuther H., Klessen R. S., Dullemond C. P., Henning T., eds, *Protostars and Planets VI*. Univ. Arizona Press, Tucson, p. 3
 Draine B. T., 2011, *Physics of the Interstellar and Intergalactic Medium*. Princeton Univ. Press, Princeton, NJ
 Draine B. T., Bertoldi F., 1996, *ApJ*, 468, 269
 Dunlop J. S. et al., 2016, preprint ([arXiv:1606.00227](https://arxiv.org/abs/1606.00227))
 Elbaz D. et al., 2011, *A&A*, 533, A119
 Elmegreen B. G., Elmegreen D. M., 1987, *ApJ*, 320, 182
 Farrah D. et al., 2013, *ApJ*, 776, 38
 Feldmann R., Hopkins P. F., Quataert E., Faucher-Giguère C.-A., Kereš D., 2016, *MNRAS*, 458, L14
 Ferland G. J. et al., 2013, *Rev. Mex. Astron. Astrofis.*, 49, 137
 Fischer J., Abel N. P., González-Alfonso E., Dudley C. C., Satyapal S., van Hoof P. A. M., 2014, *ApJ*, 795, 117

- Geach J. E., Smail I., Moran S. M., MacArthur L. A., Lagos C. d. P., Edge A. C., 2011, *ApJ*, 730, L19
- Geach J. E. et al., 2016, *ApJ*, 832, 37
- Genzel R. et al., 2012, *ApJ*, 746, 69
- George R. D. et al., 2013, *MNRAS*, 436, L99
- Glover S. C. O., Clark P. C., 2012, *MNRAS*, 421, 116
- Glover S. C. O., Mac Low M.-M., 2007, *ApJS*, 169, 239
- Glover S. C. O., Mac Low M.-M., 2011, *MNRAS*, 412, 337
- Goldsmith P. F., 2001, *ApJ*, 557, 736
- Goldsmith P. F., Langer W. D., Pineda J. L., Velusamy T., 2012, *ApJS*, 203, 13
- González-Alfonso E. et al., 2013, *A&A*, 550, A25
- Graciá-Carpio J. et al., 2011, *ApJ*, 728, L7
- Gullberg B. et al., 2015, *MNRAS*, 449, 2883
- Hailey-Dunsheath S., Nikola T., Oberst T., Parshley S., Stacey G. J., Farrah D., Benford D. J., Staguhn J., 2008, in Kramer C., Aalto S., Simon R., eds, *EAS Publ. Ser. Vol. 31, ZEUS Detection of [CII] at $z = 1.12$* . p. 159
- Herrera-Camus R. et al., 2015, *ApJ*, 800, 1
- Heyer M., Dame T. M., 2015, *ARA&A*, 53, 583
- Indriolo N., Geballe T. R., Oka T., McCall B. J., 2007, *ApJ*, 671, 1736
- Indriolo N., Neufeld D. A., Gerin M., Geballe T. R., Black J. H., Menten K. M., Goicoechea J. R., 2012, *ApJ*, 758, 83
- Iono D. et al., 2006, *ApJ*, 645, L97
- Iverson R. J. et al., 2010, *A&A*, 518, L35
- Iverson R. J., Papadopoulos P. P., Smail I., Greve T. R., Thomson A. P., Xilouris E. M., Chapman S. C., 2011, *MNRAS*, 412, 1913
- Jaquet R., Staemmler V., Smith M. D., Flower D. R., 1992, *J. Phys. B: At. Mol. Opt. Phys.*, 25, 285
- Kennicutt R. C., Evans N. J., 2012, *ARA&A*, 50, 531
- Krumholz M. R., 2012, *ApJ*, 759, 9
- Krumholz M. R., 2013a, *MNRAS*,
- Krumholz M. R., 2013b, *Astrophysics Source Code Library*, record ascl:1304.007
- Krumholz M. R., 2014, *Phys. Rep.*, 539, 49
- Krumholz M. R., Tan J. C., 2007, *ApJ*, 654, 304
- Krumholz M. R., McKee C. F., Tumlinson J., 2008, *ApJ*, 689, 865
- Krumholz M. R., McKee C. F., Tumlinson J., 2009a, *ApJ*, 693, 216
- Krumholz M. R., McKee C. F., Tumlinson J., 2009b, *ApJ*, 699, 850
- Krumholz M. R., Leroy A. K., McKee C. F., 2011, *ApJ*, 731, 25
- Krumholz M. R., Dekel A., McKee C. F., 2012, *ApJ*, 745, 69
- Launay J.-M., Roueff E., 1977, *J. Phys. B: At. Mol. Phys.*, 10, 879
- Leech K. J. et al., 1999, *MNRAS*, 310, 317
- Leroy A. K. et al., 2013, *AJ*, 146, 19
- Luhman M. L. et al., 1998, *ApJ*, 504, L11
- Luhman M. L., Satyapal S., Fischer J., Wolfire M. G., Sturm E., Dudley C. C., Lutz D., Genzel R., 2003, *ApJ*, 594, 758
- Lutz D., 2014, *ARA&A*, 52, 373
- Mashian N. et al., 2015, *ApJ*, 802, 81
- McCall B. J., Geballe T. R., Hinkle K. H., Oka T., 1999, *ApJ*, 522, 338
- McKee C. F., Krumholz M. R., 2010, *ApJ*, 709, 308
- McKee C. F., Ostriker E. C., 2007, *ARA&A*, 45, 565
- Madau P., Dickinson M., 2014, *ARA&A*, 52, 415
- Maiolino R. et al., 2005, *A&A*, 440, L51
- Malhotra S. et al., 1997, *ApJ*, 491, L27
- Malhotra S. et al., 2001, *ApJ*, 561, 766
- Muñoz J. A., Furlanetto S. R., 2013a, preprint ([arXiv:1309.6636](https://arxiv.org/abs/1309.6636))
- Muñoz J. A., Furlanetto S. R., 2013b, *MNRAS*, 435, 2676
- Muñoz J. A., Oh S. P., 2015, preprint ([arXiv:1510.00397](https://arxiv.org/abs/1510.00397))
- Murphy E. J. et al., 2011, *ApJ*, 737, 67
- Nagamine K., Wolfe A. M., Hernquist L., 2006, *ApJ*, 647, 60
- Narayanan D., Davé R., 2012, *MNRAS*, 423, 3601
- Narayanan D., Krumholz M. R., 2014, *MNRAS*, 442, 1411
- Narayanan D. et al., 2010, *MNRAS*, 407, 1701
- Narayanan D., Cox T. J., Hayward C. C., Hernquist L., 2011a, *MNRAS*, 412, 287
- Narayanan D., Krumholz M., Ostriker E. C., Hernquist L., 2011b, *MNRAS*, 418, 664
- Narayanan D., Krumholz M. R., Ostriker E. C., Hernquist L., 2012a, *MNRAS*, 421, 3127
- Narayanan D., Bothwell M., Davé R., 2012b, *MNRAS*, 426, 1178
- Narayanan D. et al., 2015, *Nature*, 525, 496
- Nelson R. P., Langer W. D., 1999, *ApJ*, 524, 923
- Neufeld D. A. et al., 2010, *A&A*, 521, L10
- Nikola T., Genzel R., Herrmann F., Madden S. C., Poglitsch A., Geis N., Townes C. H., Stacey G. J., 1998, *ApJ*, 504, 749
- Olsen K. P., Greve T. R., Narayanan D., Thompson R., Toft S., Brinch C., 2015, *ApJ*, 814, 76
- Osterbrock D. E., Ferland G. J., 2006, *Astrophysics of Gaseous Nebulae and Active Galactic Nuclei*. University Science Books, Sausalito, CA
- Pallottini A., Gallerani S., Ferrara A., Yue B., Vallini L., Maiolino R., Feruglio C., 2015, *MNRAS*, 453, 1898
- Papadopoulos P. P., 2010, *ApJ*, 720, 226
- Pineda J. L., Langer W. D., Goldsmith P. F., 2014, *A&A*, 570, A121
- Popping G., Pérez-Beaupuits J. P., Spaans M., Trager S. C., Somerville R. S., 2014, *MNRAS*, 444, 1301
- Rawle T. D. et al., 2013, preprint ([arXiv:1310.4090](https://arxiv.org/abs/1310.4090))
- Rawle T. D. et al., 2014, *ApJ*, 783, 59
- Riechers D. A. et al., 2013, *Nature*, 496, 329
- Rigopoulou D. et al., 2014, *ApJ*, 781, L15
- Robitaille T. P., Whitney B. A., 2010, *ApJ*, 710, L11
- Rodighiero G. et al., 2011, *ApJ*, 739, L40
- Rosenberg M. J. F. et al., 2015, *ApJ*, 801, 72
- Rujopakarn W. et al., 2016, *ApJ*, 833, 12
- Saintonge A. et al., 2011, *MNRAS*, 415, 32
- Sanders D. B., Mazzarella J. M., Kim D.-C., Surace J. A., Soifer B. T., 2003, *AJ*, 126, 1607
- Sargsyan L. et al., 2012, *ApJ*, 755, 171
- Schaerer D. et al., 2015, *A&A*, 576, L2
- Schöier F. L., van der Tak F. F. S., van Dishoeck E. F., Black J. H., 2005, *A&A*, 432, 369
- Schroder K., Staemmler V., Smith M. D., Flower D. R., Jaquet R., 1991, *J. Phys. B: At. Mol. Opt. Phys.*, 24, 2487
- Shetty R., Kelly B. C., Rahman N., Bigiel F., Bolatto A. D., Clark P. C., Klessen R. S., Konstantin L. K., 2013a, *MNRAS*,
- Shetty R., Kelly B. C., Bigiel F., 2013b, *MNRAS*, 430, 288
- Spilker J. S. et al., 2014, *ApJ*, 785, 149
- Spilker J. et al., 2016, *ApJ*, 826, 112
- Stacey G. J., Geis N., Genzel R., Lugten J. B., Poglitsch A., Sternberg A., Townes C. H., 1991, *ApJ*, 373, 423
- Stacey G. J., Hailey-Dunsheath S., Ferkinhoff C., Nikola T., Parshley S. C., Benford D. J., Staguhn J. G., Fiolet N., 2010, *ApJ*, 724, 957
- Staemmler V., Flower D. R., 1991, *J. Phys. B: At. Mol. Opt. Phys.*, 24, 2343
- Swinbank A. M. et al., 2012, *MNRAS*, 427, 1066
- Vallini L., Gallerani S., Ferrara A., Baek S., 2013, *MNRAS*, 433, 1567
- Vallini L., Gallerani S., Ferrara A., Pallottini A., Yue B., 2015, *ApJ*, 813, 36
- Valtchanov I. et al., 2011, *MNRAS*, 415, 3473
- van Dishoeck E. F., Black J. H., 1988, *ApJ*, 334, 771
- Venemans B. P. et al., 2012, *ApJ*, 751, L25
- Wagg J. et al., 2012, *ApJ*, 752, L30
- Wang R. et al., 2013, *ApJ*, 773, 44
- Wiesenfeld L., Goldsmith P. F., 2014, *ApJ*, 780, 183
- Willott C. J., Omont A., Bergeron J., 2013, *ApJ*, 770, 13
- Wolfire M. G., Hollenbach D., Tielens A. G. G. M., 1989, *ApJ*, 344, 770
- Wolfire M. G., McKee C. F., Hollenbach D., Tielens A. G. G. M., 2003, *ApJ*, 587, 278
- Wolfire M. G., Hollenbach D., McKee C. F., 2010, *ApJ*, 716, 1191
- Yang B., Stancil P. C., Balakrishnan N., Forrey R. C., 2010, *ApJ*, 718, 1062

APPENDIX A: RESOLUTION TESTS

Our fiducial model clouds are subdivided into 16 radial zones. In Fig. B1, we test the convergence properties of this model by varying the number of zones from 4 to 24 for a model galaxy of $\log(M_{\text{gal}}) = 9.5 M_{\odot}$. While differences exist at the lowest [CII] luminosities between $N_{\text{zone}} = 16$ and 24, they are minor.

APPENDIX B: CORRELATION WITH FIR COLOURS

Malhotra et al. (2001) and Luhman et al. (2003) find a strong correlation between the [C II]/FIR luminosity ratio in galaxies and the FIR colours (i.e. the 60/100 μm luminosity ratio).

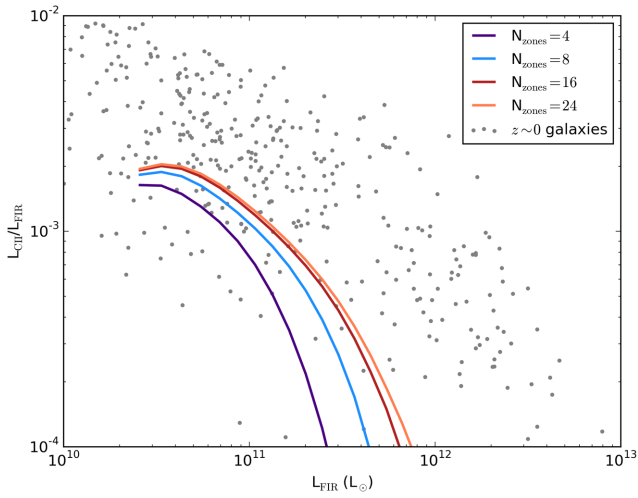


Figure B1. Convergence test for a number of radial zones in model clouds. Test shows model [C II]–FIR deficit for a galaxy of mass $M_{\text{gal}} = 3 \times 10^9 M_{\odot}$, the average mass (in log space) of our low-redshift galaxy mass range.

This paper has been typeset from a $\text{\TeX}/\text{\LaTeX}$ file prepared by the author.